Determining the surface ground state in YbB_6 and developing ultra-sensitive nanoscale dissipation measurements in scanning probe microscopy

A DISSERTATION PRESENTED
BY
AARON JOSHUA COE
TO
THE DEPARTMENT OF PHYSICS, HARVARD KENNETH C. GRIFFIN GRADUATE SCHOOL
OF ARTS AND SCIENCES

IN PARTIAL FULFILLMENT OF THE REQUIREMENTS
FOR THE DEGREE OF
DOCTOR OF PHILOSOPHY
IN THE SUBJECT OF
PHYSICS

HARVARD UNIVERSITY
CAMBRIDGE, MASSACHUSETTS
NOVEMBER 2025

Thesis advisor: Professor Jennifer Hoffman Aaron Joshua Coe

Determining the surface ground state in YbB_6 and developing ultra-sensitive nanoscale dissipation measurements in scanning probe microscopy

Abstract

My Ph.D. research comprised two main focuses: (1) the analysis of surface states in YbB_6 using scanning tunneling microscopy (STM) and spectroscopy (STS) to determine its ground state and resolve discrepancies in angle-resolved photoemission spectroscopy (ARPES) measurements, and (2) the design and construction of a novel scanning probe microscope (SPM) to expand the lab's capabilities from STM into ultra-sensitive atomic force microscopy (AFM) for both force and dissipation studies.

The first chapter provides an introduction and overview of the STM and AFM techniques and their implementation. Chapter 2 presents my work on YbB_6, which is published in its entirety as:

> Aaron Coe, Zhi-Huai Zhu, Yang He, Dae-Jeong Kim, Zachary Fisk, Jason D. Hoffman, and Jennifer E. Hoffman, "Nanoscale Conducting and Insulating Domains on YbB_6," *Physical Review Letters* **134**, 236205 (2025).

ARPES measurements have disagreed on the ground state of YbB_6 on the (001) surface. This discrepancy arises largely from the complex surface structure, caused by the absence of a natural cleavage plane and the presence of polarized terminations. Together these effects produce a disordered surface with nanoscale variations in band bending. As a result, the band structure appears smeared in spatially averaging techniques, and spectral features vary across the surface and over time. An atomically resolved technique is therefore required to identify pristine terminations and determine their elemental identity. Using STM/STS, we achieved this and proposed a ground state incorporating Rashba spin-splitting that reconciles the conflicting ARPES results.

The third chapter describes the development of a novel millikelvin SPM implementing STM and two AFM modalities. The most intriguing emergent behaviors of quantum materials are determined not only by their static band structure, but by the dynamics of their quasiparticle interactions. For example, various quantum critical fluctuations may drive unconventional superconductivity, while spin fluctuations may drive exotic topological phases. Such dynamics are largely invisible to conventional scanning tunneling microscopy (STM), while ultrafast optics typically average over the spatial variations that are common to strongly correlated materials. We have developed a unique scanning probe microscope (SPM) combining STM and pendulum atomic force microscopy (pAFM) operating below 100 mK in magnetic fields up to 14 Tesla. Atomic-scale fluctuation-dissipation dynamics are quantified by local shifts in resonance frequency (reflecting tip-sample force) and quality factor (indicating dissipation) of a scanned cantilever oscillating like a tiny pendulum above the sample [1]. Our pAFM flexibly employs a qPlus sensor [2] with custom cryogenic preamplifier, or an optically detected soft-silicon cantilever for improved force and power resolution. This manuscript is in preparation.

Contents

Listing of figures

List of Tables

Acknowledgments

The Ph.D. has been a six-year journey that truly began over twenty years ago when I received a kit for building a remote-controlled airplane. Watching that plane lift off the ground marked the beginning of a lifelong desire to understand how the world works in order to achieve extraordinary feats. In college, I took my first condensed matter course, an introduction to solid-state physics and band structure engineering taught by Prof. Nathan Lindquist at Bethel University. That class ignited my pursuit of condensed matter research, leading to work on terahertz measurements in carbon nanotubes at Osaka University under Prof. Masayoshi Tonouchi with graduate mentor Renee Bagsican Filchito, and spintronic device fabrication at Cornell University under Prof. Dan Ralph, alongside graduate mentor Jonathan Gibbons.

At Harvard University, I encountered a level of research unlike anything I had experienced before, working at lower temperatures and with equipment of far greater complexity and precision. I owe immense gratitude to my advisor, Prof. Jenny Hoffman, for entrusting me with large, technically challenging projects and for her outstanding mentorship. Jenny is a brilliant physicist who cares deeply about her students and their career paths. She has been a role model for me in raising the standard to which I hold myself and in revolutionizing how I communicate science both through writing and presentations. Her emphasis on clarity in scientific communication strengthens not only her students but the scientific community as a whole by ensuring that discoveries are rigorously researched and effectively conveyed. I also thank Jenny for her generous financial support, which allowed me to focus on technical and scientific progress without distraction. It has been a privilege to be her student.

I would also like to thank my committee members, Prof. Julia Mundy and Prof. Liang Fu. I have known Julia since I first visited Harvard as a prospective student; she has been an inviting and forthright mentor ever since. Her advice on project timelines and logistics has always proven sound and, in hindsight, remarkably prescient. I met Liang in 2021 while seeking a theorist for my committee. I am grateful that he agreed to serve, given his distinguished contributions to the field that I hope my own research advances, and for the valuable theoretical perspective he brings.

I am especially thankful to Stefan Ulrich, Jason Hoffman, and Dilek Yildiz. Since late 2020, Stefan's deep technical insight has been foundational to my dissertation. His experience as an experimental physicist guided me through the many challenges of instrument design and construction, and his systematic approach to problem-solving has shaped how I will tackle technical projects throughout my career. Jason has been essential to both the daily operations of the lab and my scientific writing. I could always rely on him for help with logistics, financial procedures, and equipment, and his fast, thoughtful feedback on my manuscript was invaluable. I wish him the best in his new position. I began working with Dilek at the start of my Ph.D., drawing on her expertise with silicon-based AFM in the pendulum geometry. Her advice on experimental focus and construction priorities was consistently insightful, and her continued availability and guidance over the years have been deeply appreciated.

I also extend my sincere thanks to the facilities staff and contractors in the Laboratory for Integrated Science and Engineering especially Bobby Kinney, Sean Concannon, Steve Concannon, Alejandro Lopez, Steve Sansone, Joe Sears, Larry O'Connell, and Joel Day. The technical scope of my

Ph.D. required extensive assistance in moving large equipment, constructing cranes, redoing wiring, adding plumbing, and building lead-loaded tables, among many other tasks. Their skill and support made this work possible, and their encouragement helped me navigate the challenges of such a large, collaborative project.

I am grateful to my colleagues in the Hoffman group for their constant support, advice, and camaraderie. They made the Ph.D. both educational and enjoyable. My deepest thanks go to Kevin Hauser, who trained me in ultrahigh vacuum technology and served as my first hands-on mentor in the group. His carefulness in design, prototyping, and operation established the mindset required to handle sensitive STM equipment. I also thank Benjamin November, who worked closely with me to build the millikelvin scanning probe microscope. His collaboration and willingness to share ideas made an intimidating project manageable. I am grateful as well to Ruizhe Kang, who taught me most of what I know about STM measurements and consistently offered valuable guidance. Ruizhe was also a great friend and source of encouragement during difficult debugging and analysis sessions. I thank Christian Matt for his early guidance, and Harry Pirie for his advice and encouragement. I also appreciate Wan-Ting Liao and Gal Tuvia. Wan-Ting began her postdoc in the group when I started my Ph.D. and, as she developed a unique four-probe STM, her parallel experiences and understanding were invaluable. Gal joined during my final year but made a strong impact on commissioning the millikelvin microscope and brought great energy to the lab. I am also grateful to have worked alongside Anjola Bamtefa, Henry Bowman, Tan Dao, Larissa Little, Alyson Spitzig, and many other exceptional members of the Hoffman lab.

I want to thank the undergraduate researchers who worked with me over the years on a variety of projects. Their efforts made possible progress that I could not have achieved alone. I especially acknowledge Federico Maccagno, who collaborated with me for several semesters and summers on constructing components for the AFM interferometer. His precision, curiosity, and ability to learn quickly were invaluable and accelerated our progress immensely.

I express my deepest gratitude to my family and friends outside the lab. My mother, Darlinda Coe, has given me unconditional love and support and was the one who gifted me that first remote-controlled airplane. She has remained a constant presence through every challenge. My sister has been both an incredible role model and an expert resource pursuing her Ph.D. in STM in Eva Andrei's group at Rutgers University during my own doctoral work. Her guidance has helped me navigate every academic stage, from high school to graduate school. I am deeply grateful to my grandfather for his unwavering support and encouragement and as a role model of a strong work ethic and unwavering integrity, which have shaped my life and career. To my friends Richard Liebert, Mairead Solvang, Kallai Hokanson, Mitch Gamburg, ZhenCheng Jiang, Joshua Kolbow, Helena Snowder, Barbara Bates, Peter Keeley, Tal Usvyatsky, and Liam DeVoe—thank you for the laughter, adventures, and countless memories that made these years so meaningful.

Lastly, I want to thank the supporting grant agencies that made these research pursuits possible. The YbB_6 imaging project was supported on AFOSR MURI FA9550-21-1-0429 and the milliKelvin microscope construction by the Gordon & Betty Moore Foundation, grant GBMF10215.

1

Introduction to methods

My six-year Ph.D. focused on the use and development of scanning probe microscopy for studying novel quantum materials. A detailed understanding of scanning tunneling microscopy (STM) and atomic force microscopy (AFM) was essential to the success of this work. In this chapter, I provide an overview of the instrumentation techniques central to my research.

1.1 Scanning Tunneling Microscopy

This dissertation primarily presents datasets acquired using STMs custom-built in the Hoffman group at Harvard University (Fig. 1.1(a)). STM achieves atomic-scale resolution through the quantum tunneling effect. As illustrated in Fig. 1.1(b), this effect allows lower energy particles to penetrate a higher level energy barrier, a behavior forbidden by classical mechanics. The particle wavefunction can be expressed for the three spatial regions as

$$\psi(z) = \begin{cases} Ae^{ikz} + Be^{-ikz}, & z < 0 \quad \text{(region I)}, \\ Ce^{-\kappa z} + De^{\kappa z}, & 0 \le z \le d \quad \text{(region II)}, \\ Fe^{ikz}, & z > d \quad \text{(region III)}. \end{cases} \tag{1.1}$$

where $k = \sqrt{2mE}/\hbar$ is the wavevector in the classically allowed regions, $\kappa = \sqrt{2m(U_0 - E)}/\hbar$ is the decay constant inside the potential barrier, E is the particle energy, U_0 is the barrier height, m is the electron mass, and $\hbar$ is the reduced Planck constant. The tunneling probability depends exponentially on the width of the potential barrier. STM exploits this sensitivity using the circuit shown in Fig. 1.1(c), where the current between the tip and the sample must tunnel through the vacuum barrier. Because the tunneling current decays exponentially with tip–sample separation, sub-ångström height sensitivity and atomic spatial resolution are achievable.

To enable scanning, either the tip or the sample is mounted on a piezoelectric tube scanner capable of bending in the x and y directions and extending in z. This scanner rasters the tip (or sample) across the surface while maintaining a vacuum gap smaller than 1 nm to sustain tunneling. Topographic imaging is typically performed in *constant-current* mode, in which a feedback loop continuously adjusts the tip height to keep the tunneling current constant. This mode is preferred over *constant-height* mode because sample inhomogeneity can cause tip crashes that degrade tip sharp-

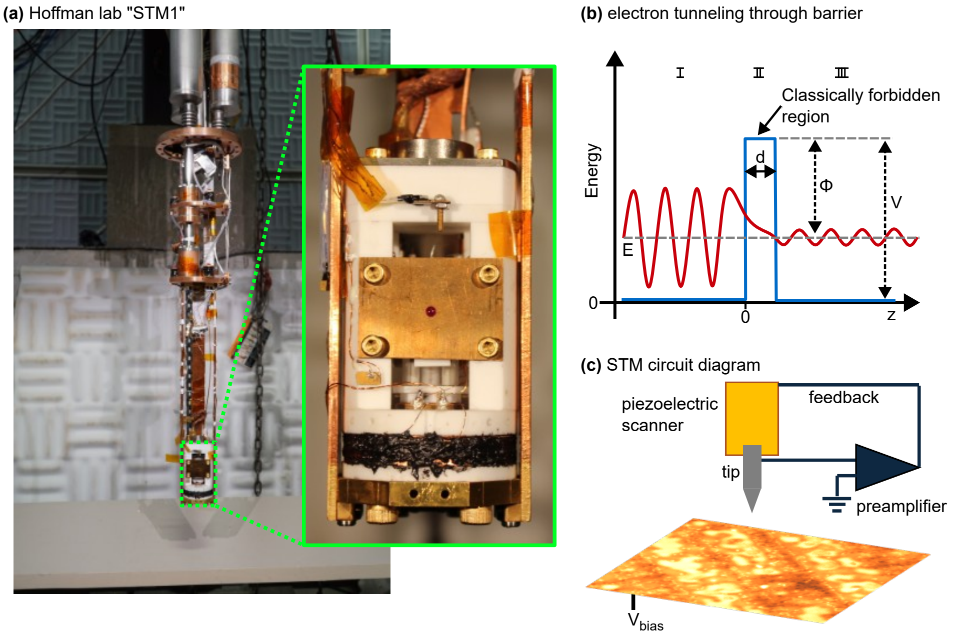

Figure 1.1: **(a)** Photo of the first STM built in the Hoffman lab. The STM is housed within a double-walled room and supported by a two-stage pneumatic isolation system. The STM head, shown in the inset, is located at the bottom of the cryostat, where it can be submerged in liquid helium to reach 4.2 K. **(b)** Schematic of electron tunneling through a one-dimensional potential barrier. The electron originates in region I, tunnels through region II, and exits into region III. **(c)** Simplified circuit diagram of the STM feedback loop for constant-current imaging. The STM tip is made atomically sharp via field emission and brought into tunneling feedback with the sample using a piezoelectric scan tube.

ness. The tradeoff, however, is slower scan speed due to the feedback response time.

It is important to note that STM topography does not represent the true geometric height of the surface. Instead, it is a convolution of the tip and sample local density of states and the tunneling transmission probability. Consequently, the apparent height can vary with imaging conditions, electronic structure, and surface reconstruction.

1.1.1 Tunneling in STM

There is additional richness in the tunneling process beyond the simple one-dimensional quantum well model. In the energy-dependent Bardeen tunneling approximation at finite temperature, the tunneling current is given by

$$I = \frac{4\pi e}{\hbar} \int_{-\infty}^{\infty} \{f(\varepsilon - eV) - f(\varepsilon)\} \rho_{\text{tip}}(\varepsilon - eV) \rho_{\text{sample}}(\varepsilon)\, T(\varepsilon, V, d)\, d\varepsilon. \tag{20.65}$$

I is the tunneling current between the tip and sample, e is the elementary charge, $f(\varepsilon)$ is the Fermi–Dirac distribution function at energy ε, V is the applied bias voltage between the tip and sample, $\rho_{\text{tip}}(\varepsilon)$ and $\rho_{\text{sample}}(\varepsilon)$ are the electronic density of states of the tip and sample, respectively, $T(\varepsilon, V, d)$ is the tunneling transmission probability, which depends on energy, bias, and tip–sample separation d, m is the electron mass, and Φ_{tip} and Φ_{sample} are the work functions of the tip and sample, respectively. In the one-dimensional approximation, the transmission probability can be expressed as

$$T(\varepsilon, V, d) \propto \exp\left[-2d\sqrt{\frac{2m}{\hbar^2}\left(\frac{\Phi_{\text{tip}}+\Phi_{\text{sample}}}{2} + \frac{eV}{2} - \varepsilon\right)}\,\right]. \tag{1.2}$$

This model was originally developed for metal–insulator–metal tunneling junctions but is equally applicable to the STM tunneling process. It treats the tip and sample as independent systems, with transitions between their electronic states described using time-dependent perturbation theory. The process is illustrated in Fig. 1.2, where an applied sample bias shifts the Fermi level, revealing empty electronic states in the sample into which tip electrons can tunnel.

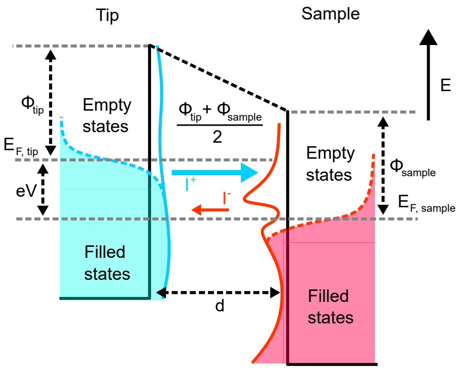

Figure 1.2: Illustration of tip-to-sample tunneling with a negative bias applied to the tip. The tip wavefunction is nearly constant and broadened near the Fermi level by the Fermi function. The sample density of states contains local features and is also thermally broadened. The difference in Fermi levels produces a net tunneling current from the tip into the sample.

1.1.2 SCANNING TUNNELING SPECTROSCOPY

Because the tunneling current depends on the sample's electronic density of states, it is possible to obtain energy-resolved information at the atomic scale through scanning tunneling spectroscopy (STS). STS measures the derivative of the tunneling current with respect to the applied voltage, denoted as dI/dV, yielding

$$\frac{dI}{dV}\frac{\hbar}{4\pi e} = e\rho_{\text{tip}}\rho_{\text{sample}}(eV)\, T(eV, V) + \int_0^{eV} \rho_{\text{tip}}\rho_{\text{sample}}(\varepsilon)\, \frac{\partial T(\varepsilon, V)}{\partial V}\, d\varepsilon. \tag{1.3}$$

In the one-dimensional approximation, the transmission probability is given by

$$T(\varepsilon, V, d) \propto \exp\left[-2d\sqrt{\frac{2m}{\hbar^2}\left(\bar{\Phi} + \frac{eV}{2} - \varepsilon\right)}\,\right]. \tag{1.4}$$

where $\bar{\Phi} = (\Phi_{\text{tip}} + \Phi_{\text{sample}})/2$ is the average tunneling barrier height.

Here, thermal broadening has been neglected for simplicity. When STS is performed near the Fermi level, the transmission factor is approximately constant, and if the tip's density of states is also energy-independent, the expression simplifies to

$$\frac{dI}{dV} \propto \rho_{\text{sample}}(eV). \tag{1.5}$$

Thus, under these assumptions, the differential conductance is directly proportional to the sample's local density of states. This relationship forms the basis for qualitative interpretation of STS measurements in most tunneling experiments.

1.1.3 Lock-in Technique

To perform STS, the tip is positioned above the sample, and feedback is established at a set tunneling current and sample bias. Feedback is then disabled, and the dI/dV signal is recorded. To obtain the derivative of the current, a modulation (lock-in) technique is employed, where

$$I = f(V) \tag{1.6}$$

If a small AC modulation is added to the bias, then

$$I(t) = f(V + V_M \cos \omega t)\,. \tag{1.7}$$

V_M is the amplitude of the modulation voltage applied to the sample bias, ω is the angular frequency of the applied modulation voltage, and t is the time variable describing the temporal evolution of the modulation signal. For sufficiently small modulation voltages, the amplitude detected by the lock-in amplifier is proportional to dI/dV. This relationship is illustrated in Fig. 1.3(a), where the oscillation amplitude of the current signal is proportional to the slope of the I–V curve, and the energy resolution of the measured signal is determined by the modulation amplitude. A more rigorous derivation is obtained by performing a Taylor expansion of I around the voltage V:

$$
\begin{aligned}
I = \sum_{k=0}^{\infty} \frac{V_M^k}{k!}\frac{d^k f(V)}{dV^k}\cos^k(\omega t) &= \left[f(V) + \frac{d^2 f(V)}{dV^2}\frac{V_M^2}{4} + \cdots \right] \\
&+ \left[\frac{df(V)}{dV} + \frac{d^3 f(V)}{dV^3}\frac{V_M^2}{8} + \cdots \right] V_M \cos(\omega t) \\
&+ \left[\frac{d^2 f(V)}{dV^2} + \frac{d^4 f(V)}{dV^4}\frac{V_M^2}{12} + \cdots \right] \frac{V_M^2}{2} \cos(2\omega t) \\
&+ \left[\frac{d^3 f(V)}{dV^3} + \frac{d^5 f(V)}{dV^5}\frac{V_M^2}{20} + \cdots \right] \frac{V_M^3}{4!} \cos(3\omega t) + \cdots
\end{aligned}
\tag{1.8}
$$

This result shows that the *n*th derivative of the current can be extracted by detecting the signal component at *n* times the modulation frequency, assuming higher-order terms in each bracket are negligible.

Focusing only on the dominant terms, the current signal can be approximated as

$$I_{\text{sig}} \sim I(V) + V_m \frac{dI}{dV}\cos\omega t \tag{1.9}$$

However, the total current also contains noise contributions:

$$I_{\text{tot}} = I_{\text{sig}} + I_{\text{noise}} = I(V) + V_m \frac{dI}{dV}\cos\omega t + \sum_j I_j \cos(\omega_j t) \tag{1.10}$$

Because the lock-in amplifier measures voltage signals, the corresponding lock-in output (given $V_{tot} \sim I_{tot}$) is written as

$$V_{\text{out}} = \frac{1}{T}\int_0^t V_{\text{tot}}(\tau)\, V_{\text{ref}}(\tau)\, d\tau \tag{1.11}$$

where

$$V_{ref} = cos(\omega\tau + \theta). \tag{1.12}$$

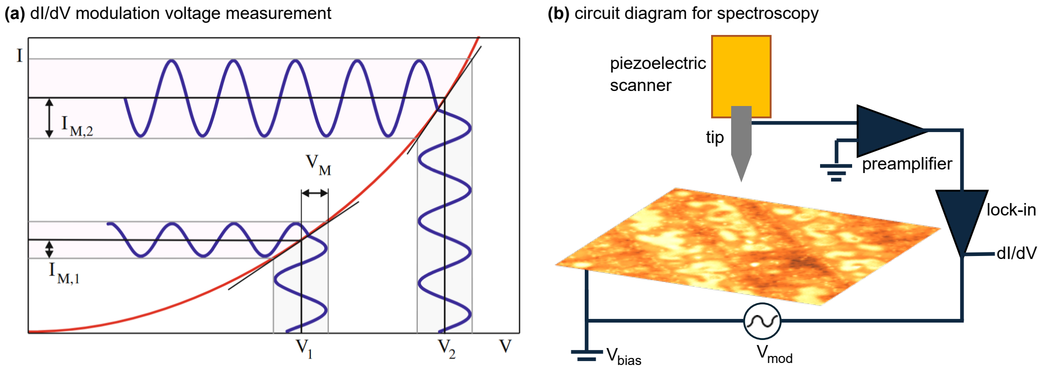

(a) dI/dV modulation voltage measurement

(b) circuit diagram for spectroscopy

Figure 1.3: (a) Principle of differential conductance measurement using a small modulation voltage V_M adapted from Voigtländer[1]. A sinusoidal bias modulation is applied to the tunneling voltage, producing an oscillating current whose amplitude I_M is proportional to the slope of the I–V curve at the corresponding bias. The energy resolution of the measurement is determined by the modulation amplitude. **(b)** Simplified circuit diagram for STM. A small AC modulation V_{mod} is added to the DC sample bias V_{bias}, and the resulting current is amplified and demodulated by a lock-in amplifier to obtain the differential conductance *dI/dV*.

V_{ref} is the lock-in reference voltage at frequency ω and phase offset θ. Performing this integration, while considering the orthogonality of sinusoidal functions, yields

$$V_{out} = \frac{V_m}{2}\frac{dI}{dV}\cos\theta + V_{\omega}^{\text{noise}} \qquad (1.13)$$

$V_{\omega}^{\text{noise}}$ is the residual noise voltage component at the lock-in detection frequency. Thus, only the noise components at the specific lock-in reference frequency are retained. It is therefore essential to choose a lock-in frequency where the noise level is low and the frequency is sufficiently high to maximize both signal-to-noise ratio and measurement speed. A circuit diagram for STS is illustrated in Fig. 1.3(b).

1.1.4 Energy resolution and experimental limits

There are three primary contributions to energy smearing in STS measurements: the transmission factor, thermal broadening from the Fermi functions, and the modulation amplitude of the lock-in technique. The transmission factor becomes significant only at large bias voltages (on the order of several volts), where it dominates and limits the energy resolution to several hundred meV. At low voltages, both the Fermi functions and the modulation amplitude determine the effective thermal energy smearing. For small bias voltages (hundreds of meV or less), the differential conductance can be simplified to

$$\frac{dI}{dV} = \frac{4\pi e}{\hbar} T(d)\rho_{\text{tip}} \int_{-\infty}^{\infty} \frac{\partial f(\varepsilon - eV)}{\partial V} \rho_{\text{sample}}(\varepsilon)\, d\varepsilon \tag{1.14}$$

The slope of the Fermi function near the Fermi level is

$$\left.\frac{\partial f(\varepsilon - eV)}{\partial V}\right|_{\varepsilon = eV} = -\frac{1}{2k_B T} \tag{1.15}$$

This results in an approximate thermal broadening of $\sim\ 4k_B T$ for a delta-function density of states. For Gaussian-shaped spectral features, the full width at half maximum (FWHM) of the thermal broadening is approximately $3.2k_B T$. This corresponds to a peak width of 0.28 meV/K, or equivalently 83 meV at room temperature, 1.2 meV at 4 K, 28 μeV at 100 mK, and 2.8 μeV at 10 mK. Clearly, reducing temperature greatly enhances the ability of STS to resolve fine electronic features such as the superconducting gaps in NbSe_2 [2] or the zero-bias Majorana signatures observed in Fe(Te,Se) vortex cores.[3]

The final contribution to energy broadening arises from the lock-in modulation voltage. The effective broadening is approximately twice the root-mean-square (RMS) modulation voltage, $2V_{\text{mod,RMS}}$. Thus, the total low-bias energy broadening can be approximated as

$$\Delta E = \sqrt{(2eV_{\text{mod,RMS}})^2 + (0.28\,\text{meV/K} \cdot T)^2}. \tag{1.16}$$

At 4 K, thermal broadening typically dominates, whereas at millikelvin temperatures the modulation voltage becomes the primary factor limiting energy resolution.

1.2 ATOMIC FORCE MICROSCOPY

AFM was developed in 1986 following the invention of STM. The technique is conceptually similar: a sharp tip is rastered across the sample surface using a piezoelectric scan tube under feedback control. However, in AFM the measured signal is the force between the tip and the sample rather than a tunneling current. To detect these forces, the bending or oscillatory motion of a microcantilever must be monitored. Early AFM implementations used an STM to detect cantilever deflection,[4] but STM proved unsuitable for this task, motivating the development of several alternative detection schemes. Over time, AFM has evolved to measure a wide range of interaction forces using diverse operational modes and cantilever designs, achieving atomic-scale resolution even on materials inaccessible to STM.[5,6] In the following section, I discuss the fundamental principles of AFM, the evolution of its detection schemes, and its broader applications beyond direct tip–sample force measurements.

1.2.1 HARMONIC OSCILLATORS

Harmonic oscillators are among the most versatile and widely applicable models for describing dynamics in nature. They capture phenomena ranging from phonon vibrations in solids and molecular bond stretching to electrical LC circuits, optical cavity modes, and the motion of mechanical resonators such as AFM cantilevers. In the simplest case, a harmonic oscillator is described by the differential equation

$$ma = m\frac{d^2z}{dt^2} = m\ddot{z} = F = -kz. \tag{1.17}$$

k is the spring constant, where m is the effective mass of the oscillator, $\ddot{z}$ is its acceleration, and $\dot{z}$ is the velocity. This has the general solution

$$z = A\cos(\omega_0 t) + B\sin(\omega_0 t). \tag{1.18}$$

where $\omega_0 = \sqrt{k/m}$ is the natural angular frequency of the oscillator.

Including both a damping term and an external driving force makes the model more representative of real systems:

$$m\ddot{z} = -m\gamma\dot{z} - k(z - z_{\text{drive}}). \tag{1.19}$$

γ is the damping coefficient and z_{drive} is the displacement of the external driving source. This has the steady-state solution

$$z = A\cos(\omega t + \varphi), \tag{1.20}$$

where the amplitude and phase are given by

$$A^2 = \frac{A_{\text{drive}}^2}{\left(1 - \frac{\omega^2}{\omega_0^2}\right)^2 + \frac{1}{Q^2}\frac{\omega^2}{\omega_0^2}}. \tag{1.21}$$

and

$$\tan\varphi = \frac{-\frac{\omega}{\omega_0}}{Q\left[1 - \left(\frac{\omega}{\omega_0}\right)^2\right]}. \tag{1.22}$$

Q is the quality factor of the oscillator, defined as $Q = \dfrac{\omega_0}{2\gamma}$, which quantifies the ratio of the stored energy to the energy dissipated per oscillation cycle and characterizes the sharpness of the resonance. This damped, driven harmonic oscillator exhibits a resonance at $\omega = \omega_0$, where the amplitude is maximal and the phase shifts by -180°, as shown in Fig. 1.4.

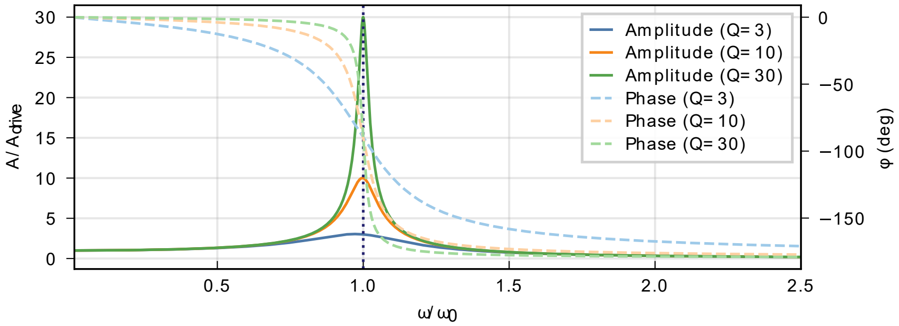

Figure 1.4: Normalized amplitude response A/A_{drive} (left vertical axis) as a function of the normalized drive frequency ω/ω_0 for different quality factors Q. Higher Q values produce sharper and higher resonance peaks. Corresponding phase response φ (right vertical axis) for the same Q values. As Q increases, the phase transition near resonance becomes steeper, approaching a total shift of -180° across the resonance frequency.

1.2.2 FORCES BETWEEN TIP AND SAMPLE

Forces between the AFM tip and the sample arise from several distinct physical interactions, including electrostatic, van der Waals, chemical, and Pauli-repulsive forces. AFM can differentiate between these interactions based on their characteristic length scales, as different forces dominate at different tip–sample separations.

The electrostatic force is the longest-range interaction and is generally attractive, arising from image charges induced in the sample by the biased tip. The tip–sample electrostatic interaction is more accurately modeled as a capacitor rather than as discrete point charges. For a spherically shaped tip interacting with a planar sample, the total electrostatic force can be expressed as

$$F_{\text{el.total}}(z) = -\pi\varepsilon_0 U^2 \left[\frac{R^2}{z(z+R)} + c^2\left(\ln\left(\frac{z+R}{h}\right) - 1 + \frac{R/\sin(\varphi)}{z+R}\right)\right]. \tag{1.23}$$

where ε_0 is the vacuum permittivity, U is the applied voltage between the tip and sample, R is the tip radius, h, is the tip height, z is the tip–sample separation, $c^2 = \frac{1}{\ln\tan(\Upsilon/2)}$, Υ is the opening angle, and φ is the half-angle of the conical tip.

The van der Waals force describes the interaction between transient dipoles of neutral atoms or molecules that arise from quantum mechanical charge fluctuations. For macroscopic objects, this force results from the sum of many pairwise interactions and is typically modeled empirically as

$$F(\vec{r}) = -\frac{dV(\vec{r})}{d\vec{r}} \rightarrow F_{\mathrm{vdW}}(\vec{r}) = -\frac{HR}{6\,\vec{r}^2}. \tag{1.24}$$

where $\vec{r}$ is the distance vector between the tip and sample, and H is the Hamaker constant that characterizes the material-dependent strength of the van der Waals interaction.

The chemical interaction potential is often used as the introductory model for short-range AFM forces. It is typically represented by the Lennard–Jones (LJ) potential, which captures both the attractive (van der Waals) and repulsive (Pauli exclusion) contributions. The attractive term scales as $1/r^6$, reflecting dispersion forces, while the repulsive term scales as $1/r^{12}$ and prevents atomic collapse. The LJ potential can be written as

$$V_{\mathrm{LJ}}(\vec{r}) = -\frac{A}{\vec{r}^6} + \frac{B}{\vec{r}^{12}}. \tag{1.25}$$

where A and B are empirical constants representing the attractive and repulsive components, respectively. A more generalized and widely used form:

$$V_{\mathrm{LJ}}(\vec{r}) = 4\varepsilon\left[\left(\frac{\sigma}{\vec{r}}\right)^{12} - \left(\frac{\sigma}{\vec{r}}\right)^{6}\right]. \tag{1.26}$$

Here $\varepsilon = A^2/4B$ and $\sigma = (B/a)^{1/6}$. The corresponding interatomic force is obtained by differentiating the potential with respect to distance:

$$F_{\mathrm{LJ}}(\vec{r}) = \frac{24\varepsilon}{\sigma}\left[\left(\frac{2\sigma}{\vec{r}}\right)^{13} - \left(\frac{\sigma}{\vec{r}}\right)^{7}\right]. \tag{1.27}$$

In these expressions, ε determines the depth of the potential well (the binding strength between atoms), and σ represents the equilibrium distance at which the potential energy is minimized.

1.2.3 CANTILEVER DETECTION STYLES

In the first implementation of AFM, an STM was used to detect the cantilever dynamics.[4] However, STM detection proved suboptimal because it was overly sensitive to torsional oscillations of the cantilever, limited the usable oscillation amplitude, and was only weakly responsive to portions of the cantilever motion due to STM's short-range tunneling regime. Several alternative detection techniques have since been developed. The most common is the optical beam deflection (OBD) method,[7] in which a laser is directed onto the back side of the cantilever and reflected onto a split photodiode. Another widely used approach is the interferometric detection technique,[8,9] where a common-path interferometer is formed at the glass–vacuum interface of an optical fiber that directs light toward the cantilever. The reflected light from both the fiber end and the cantilever surface recombines within the fiber and is guided to a photodetector. Variations in the optical path length due to cantilever motion cause phase shifts that modulate the detected optical power.

A third method, the piezoresistive technique, integrates a piezoresistive layer directly onto the cantilever; mechanical bending induces stress in this layer, changing its electrical resistance, which can be measured using a Wheatstone bridge or differential amplifier circuit. Finally, quartz-based piezoelectric cantilevers [12] have gained popularity due to their self-sensing capability, eliminating the need for optical components and offering robust, easily reproducible operation.[13]

The optical beam deflection method is the most widely adopted in laboratory AFM systems because of its simplicity, high bandwidth, and compatibility with ambient conditions. The inter-

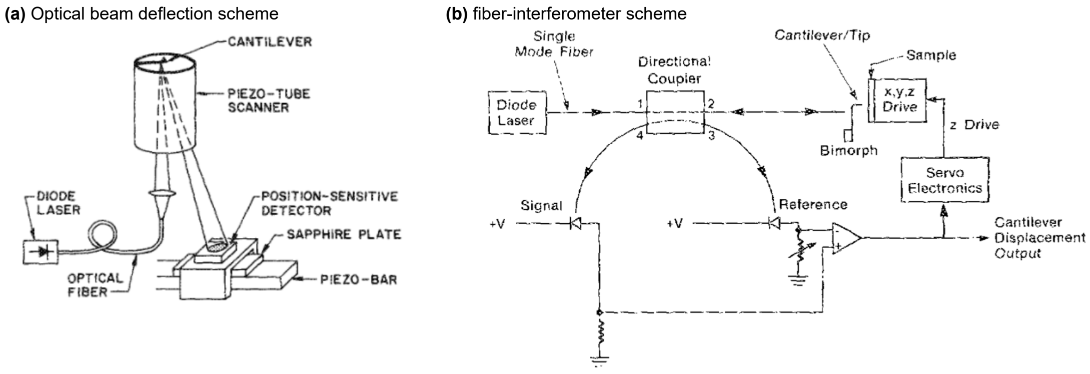
(a) Optical beam deflection scheme

(b) fiber-interferometer scheme

Figure 1.5: **(a)** Optical beam deflection scheme adapted from Meyer and Amer[10], where a diode laser is focused onto the cantilever and the reflected beam is detected by a position-sensitive detector mounted on a piezo-bar inside the UHV chamber. **(b)** Fiber-interferometer scheme from Rugar *et. al.*,[11] in which a single-mode fiber and directional coupler form a compact interferometer to measure cantilever displacement via optical interference..

ferometric method, by contrast, is particularly valuable in cryogenic environments where optical alignment, space constraints, and low electronic noise requirements limit the feasibility of beam deflection setups. The optical current generated at the photodetector for fiber–cantilever gap distances smaller than the fiber core diameter is given by

$$I = RP = R\frac{(r_1^2 + r_2^2) - 2r_1r_2\cos\delta}{(1 + r_1^2r_2^2) - 2r_1r_2\cos\delta}. \tag{1.28}$$

where R is the response (sensitivity) of the photodetector, P is the incident optical power, r_1 is the reflection coefficient at the fiber–vacuum interface, r_2 is the reflection coefficient at the cantilever surface, λ is the wavelength of the laser light, D is the distance between the fiber end and the cantilever surface, and $\delta = 4\pi D/\lambda$ is the phase difference between the two reflected beams.

The fiber interferometer can be operated in two primary modes. In the first mode, a single reflection from the cantilever surface dominates the detected signal, producing the normalized intensity pattern shown in Fig. 1.6(a). When the reflectivity r_1 is enhanced through surface preparation of the fiber end, multiple internal reflections occur, forming a Fabry–Perot type interferometer. In this regime, the power modulation becomes sharper, as illustrated in Fig. 1.6(b), which improves the signal-to-noise ratio but significantly narrows the dynamic range to several hundred ångströms[14].

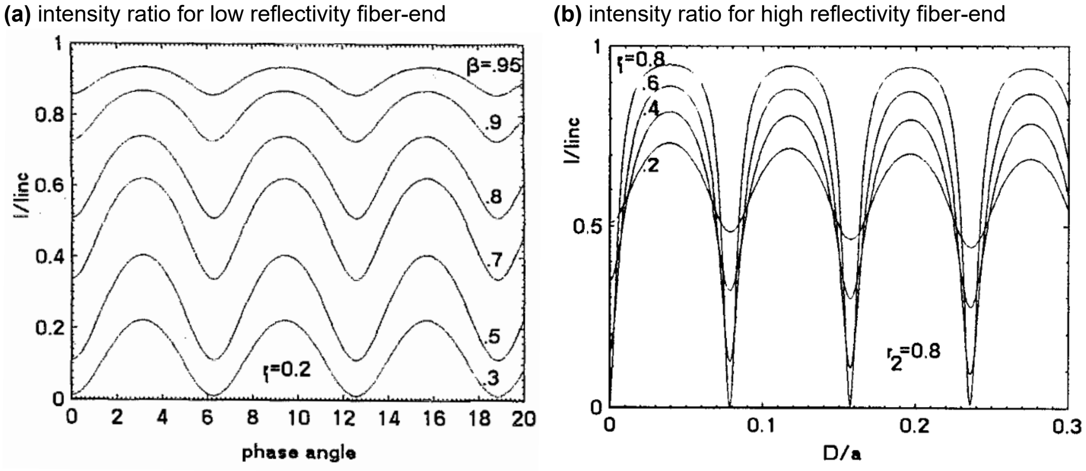

Figure 1.6: **(a)** Calculated normalized intensity ratio I/I_{inc} as a function of phase angle for a low-reflectivity fiber end. The interference pattern varies smoothly with phase, providing a broad dynamic range but lower sensitivity. **(b)** Calculated normalized intensity ratio I/I_{inc} as a function of normalized fiber–cantilever distance D/a for a high-reflectivity fiber end. Multiple reflections produce sharper Fabry–Perot–type fringes, increasing signal sensitivity but reducing the dynamic range. Figure panels adapted from Putman *et. al.*[14]

We can derive a comparison in ultimate sensitivity between OBD and optical-interferometry. The fundamental detection limits for measuring AFM cantilever displacement are governed by *diffraction* and *photon shot noise*. Other sources, including mechanical vibration, electronics, laser noise, or thermal drift, are secondary and not considered in this theoretical ideal analysis.

We first consider a interferometer, where the response varies sinusoidally with cantilever position z. At quadrature, small tip displacements Δz cause a change in the number of detected photons,

$$\Delta N = t N_{\text{tot}} \frac{2\pi}{\lambda} \Delta z, \tag{1.29}$$

where t is the measurement time, N_{tot} is the photon emission rate from the laser, and λ is the wavelength. The signal-to-noise ratio (SNR), limited by photon shot noise, is then

$$\mathrm{SNR_{int}} = (8\pi^2 t N_{\mathrm{tot}})^{1/2}\frac{\Delta z}{\lambda}. \tag{1.30}$$

Next, we consider the OBD technique. A collimated Gaussian laser beam of diameter D_0 is incident on the reflective backside of a cantilever of length l and is focused by a lens of focal length f onto a split detector. When the cantilever tilts, the reflected beam shifts laterally on the detector by

$$\Delta s = 2f\frac{\Delta z}{l}, \tag{1.31}$$

where the factor of 2 accounts for the doubled reflection angle.

In the detector's focal plane, the Gaussian intensity profile has a width

$$D_{\mathrm{sd}} = \frac{4\lambda f}{\pi D_0}. \tag{1.32}$$

The resulting photon number difference between the two detector halves is

$$\Delta N = t N_{\mathrm{tot}}(2\pi)^{1/2}\frac{D_0}{l}\frac{\Delta z}{\lambda}. \tag{1.33}$$

This gives a shot-noise-limited signal-to-noise ratio

$$\mathrm{SNR_{obd}} = (8\pi t N_{\mathrm{tot}})^{1/2}\frac{D_0}{l}\frac{\Delta z}{\lambda}. \tag{1.34}$$

For $D_0 = l$, the sensitivity ratio between the two methods is

$$\frac{\mathrm{SNR_{int}}}{\mathrm{SNR_{obd}}} = \pi^{1/2} \approx 1,$$

showing that optical beam deflection and interferometry are fundamentally equivalent in sensitivity when both operate under shot-noise and diffraction-limited conditions.

This equivalence arises because both detect phase-induced intensity shifts in the reflected optical field: interferometry through explicit interference fringes and OBD through the spatial interference of reflected rays forming the Gaussian spot on the detector. The ultimate resolution for several detection techniques are listed in Table. 1.1.

Table 1.1: Comparison of the minimum detectable cantilever displacement for various optical detection techniques. Adapted from Putman *et. al.*[15]

Technique	$(\Delta z)_{\text{min}}$
Optical beam deflection[10]	1.0×10^{-13}
Interferometry[9]	1.7×10^{-13}
Fiber interferometry[11]	5.5×10^{-14}
Laser diode feedback[15]	3.0×10^{-12}

1.2.4 Non-contact Frequency modulated AFM

AFM is commonly operated in *contact mode*, where the cantilever is physically dragged across the sample surface. As the local topography changes, the cantilever bends in response to the varying tip–sample force, and this deflection is detected optically using a photodetector. The main limitations of contact-mode AFM are that it primarily measures van der Waals forces from the surface, it can cause mechanical damage to delicate samples, and its spatial resolution is limited by the macroscopic radius of the tip apex.

For studies of quantum materials, it is typically preferable to use a *non-contact* AFM (nc-AFM) technique. The simplest and most common implementation of nc-AFM is amplitude-modulated AFM (AM-AFM), in which the cantilever is oscillated near its resonance frequency using a piezoelectric actuator. The tip–sample interaction modifies the effective spring constant of the cantilever, leading to changes in its resonance frequency. If the drive frequency is held constant, these changes appear as variations in the oscillation amplitude and phase. However, AM-AFM becomes less practical in vacuum or cryogenic conditions, where the quality factor Q of the cantilever increases by several orders of magnitude. The high Q lengthens the response time, requiring many oscillation cycles to reach a steady state at each measurement point. Under such conditions, frequency-modulated AFM (FM-AFM) is the preferred technique.

In FM-AFM, the tip–sample interaction modifies the resonance frequency of the cantilever by altering the effective spring constant through the force gradient experienced during each oscillation cycle. This approach enables the measurement of both conservative and dissipative (inelastic) components of the tip–sample interaction. The average force gradient can be directly related to the shift in resonance frequency, allowing the force profile to be reconstructed as a function of tip–sample distance. In FM-AFM, the cantilever is continuously driven at its instantaneous resonance frequency, which shifts due to the interaction with the sample. The frequency shift is proportional to the weighted average of the tip–sample force, with the largest contribution coming from the closest approach (the lower turnaround point) as shown in Fig. 1.7(a). The frequency shift can be expressed as

$$\Delta f = -\frac{f_0}{A^2 k} \left\langle F_{\mathrm{ts}}(t) \cdot z(t) \right\rangle . \tag{1.35}$$

where f_0 is the free resonance frequency of the cantilever, A is the oscillation amplitude, k is the cantilever spring constant, $F_{\mathrm{ts}}(t)$ is the instantaneous tip–sample force, and $z(t)$ is the time-dependent displacement of the cantilever.

We can define an effective tip–sample spring constant as

$$k' \equiv -\frac{2\langle F_{\mathrm{ts}} \cdot z \rangle}{A^2}, \tag{1.36}$$

The implementation of FM-AFM typically requires a phase-locked loop (PLL) to track and

(a) Force and weighting function for AFM oscillations

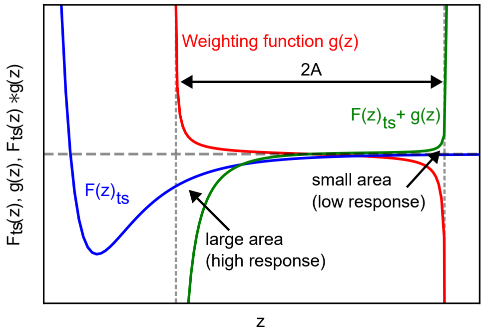

(b) afm circuit diagram

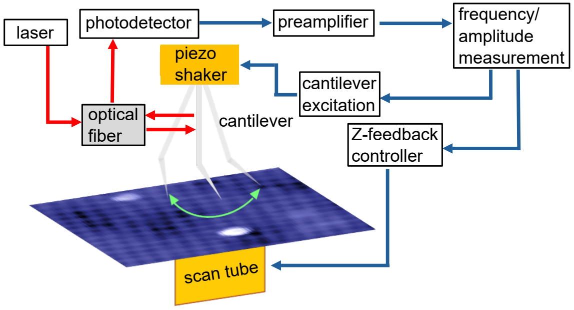

Figure 1.7: **(a)** Illustration of the tip–sample interaction force $F_{\text{ts}}(z)$ (blue) and the corresponding weighting function $g(z)$ (red) used in frequency-modulated AFM (FM-AFM). The product $F_{\text{ts}}(z)g(z)$ (green) represents the effective contribution of the force gradient to the measured frequency shift, with the strongest weighting occurring near the lower turning point of the cantilever oscillation. **(b)** Simplified block diagram of the AFM detection system. A laser coupled into an optical fiber measures cantilever motion via interferometry or beam deflection, with the resulting optical signal detected by a photodiode and amplified. The preamplifier output is processed for frequency and amplitude measurement, while feedback loops control the cantilever excitation and the Z-position of the piezo scan tube to maintain constant interaction conditions.

maintain oscillation at the instantaneous resonance frequency. The PLL continuously locks to the resonance frequency of the cantilever and adjusts the drive signal accordingly (Fig. 1.7(b)). This is especially important in low-temperature AFM, where thermal excitation of the cantilever is suppressed, and active driving is necessary to sustain oscillation. However, the use of a PLL introduces a finite response time, as the feedback must track phase variations in the cantilever signal, leading to measurement time constants on the order of hundreds of milliseconds.

The PLL operates by detecting changes in resonance frequency as phase shifts in the cantilever signal. The circuit multiplies the incoming cantilever signal, $V_{\text{cant}} \propto \cos(\omega_{\text{cant}} t)$, by a reference signal generated by a voltage-controlled oscillator (VCO), $V_{\text{vco}} \propto \cos(\omega_{\text{vco}} t + \varphi_0)$, and low-passes the result:

$$V_{\text{cant}} \cdot V_{\text{vco}} \propto \frac{1}{2} \left(\cos\left[(\omega_{\text{cant}} + \omega_{\text{vco}}) t + \varphi_0 \right] + \cos\left[(\omega_{\text{vco}} - \omega_{\text{cant}}) t + \varphi_0 \right] \right) . \tag{1.37}$$

The high-frequency term is filtered out, leaving the difference term, which depends on the time-varying phase:

$$V_{\text{phase}} \propto \cos\left[(\omega_{\text{vco}} - \omega_{\text{cant}}) t + \varphi_0 \right] = \cos(\delta\omega t + \varphi_0) = \cos(\varphi(t)), \tag{1.38}$$

The PLL converts this phase difference into a control voltage proportional to the instantaneous phase, with a proportionality constant K_{pd}. For optimal sensitivity, the operating point is maintained near 90°, allowing a small-angle approximation for $\delta\omega \ll \omega_0$:

$$V_{\text{phase}} = K_{\text{pd}} \cos(\delta\omega t + 90^\circ) \approx -K_{\text{pd}}\, \delta\omega t. \tag{1.39}$$

In summary, FM-AFM relies on frequency modulation and demodulation principles analogous to FM radio. The high-frequency oscillation of the cantilever, modulated by tip–sample interactions, is mixed with a reference signal to extract a low-frequency phase or frequency shift. This signal directly reflects the local force gradient between the tip and sample and forms the basis for quantitative AFM force spectroscopy.

1.2.5 Noise in AFM

Next, we derive the contribution of thermal noise in AFM measurements. Thermal noise sets the fundamental limit of force sensitivity and frequency stability in both contact and non-contact AFM modes. Starting with the equipartition theorem, the total average energy stored in a thermally excited harmonic oscillator is $k_B T$. Because this total energy is equally divided between kinetic and potential energy on average, the root-mean-square (RMS) thermal displacement amplitude of the cantilever can be written as

$$\left\langle \Delta z_{\mathrm{th}}^2 \right\rangle = \frac{k_B T}{k}. \tag{1.40}$$

For room temperature ($T = 300$ K) and a typical cantilever spring constant of $k = 1$ N/m, this yields a thermal displacement of approximately 20 pm. At 100 mK, the thermal excitation drops to about 7 fm, illustrating how cooling drastically suppresses thermal motion.

A more rigorous treatment models the cantilever as a harmonic oscillator coupled to a thermal bath. In this framework, thermal energy excites the cantilever motion through random forces, and the frequency response follows the resonance characteristics of the oscillator. The power spectral density (PSD) of the thermal displacement noise is given by

$$N_{\mathrm{th,osc}}(f) = N_{\mathrm{th,exc}}\, G(f) = \sqrt{\frac{2k_B T}{\pi k Q f_0}}\, G(f), \tag{1.41}$$

where $N_{\mathrm{th,exc}}$ is the frequency-independent white noise arising from the thermal excitation, and $G(f)$ is the transfer function of the harmonic oscillator, defined as

$$G^2(f) \equiv \frac{A^2}{A_{\mathrm{drive}}^2} = \frac{1}{\left(1 - \frac{f^2}{f_0^2}\right)^2 + \frac{1}{Q^2}\frac{f^2}{f_0^2}}. \tag{1.42}$$

Here, f_0 is the natural resonance frequency of the cantilever, A_{drive} is the driven oscillation amplitude, and Q is the mechanical quality factor that quantifies the damping in the oscillator.

In frequency-modulated AFM, the cantilever oscillation is detected within a two-sided bandwidth centered around f_0, i.e., between $f_0 \pm f_{\text{mod}}$. Because the modulation frequency f_{mod} is typically much smaller than f_0 ($f_{\text{mod}} \ll f_0$), we can approximate the transfer function near resonance as

$$G^2(f_0 + f_{\text{mod}}) = \frac{1}{\left(1 - \frac{(f_0+f_{\text{mod}})^2}{f_0^2}\right)^2 + \frac{1}{Q^2}\frac{(f_0+f_{\text{mod}})^2}{f_0^2}} \approx \frac{1}{4\frac{f_{\text{mod}}^2}{f_0^2} + \frac{1}{Q^2}}. \tag{1.43}$$

Thus, the thermally induced displacement noise power spectrum becomes

$$N_{z,\text{th}}^2(f_{\text{mod}}) = N_{\text{th,exc}}^2 G^2(f_0 + f_{\text{mod}}) = \frac{2k_B T}{\pi k Q f_0}\frac{1}{4\frac{f_{\text{mod}}^2}{f_0^2} + \frac{1}{Q^2}}. \tag{1.44}$$

Because the frequency noise density is related to the displacement noise density through the modulation frequency and the oscillation amplitude, we can write

$$N_{f,\text{th}}(f_{\text{mod}}) = \frac{\sqrt{2 f_{\text{mod}}}}{A} N_{z,\text{th}}(f_0 + f_{\text{mod}}). \tag{1.45}$$

where A is the oscillation amplitude of the cantilever.

Integrating the frequency noise over a measurement bandwidth B gives the mean-squared thermal frequency fluctuation

$$
\begin{aligned}
\langle \Delta f_{\mathrm{th}}^2 \rangle &= \int_0^B N_{f,\mathrm{th}}^2(f_{\mathrm{mod}})\, df_{\mathrm{mod}} \\
&= \frac{4k_B T}{\pi A^2 k Q f_0} \int_0^B \frac{f_{\mathrm{mod}}^2}{4\frac{f_{\mathrm{mod}}^2}{f_0^2} + \frac{1}{Q^2}}\, df_{\mathrm{mod}} \\
&= \frac{k_B T}{\pi A^2 k Q} \left[f_0 B - \frac{f_0^2}{2Q} \arctan\left(\frac{2QB}{f_0} \right) \right] . \qquad (1.46)
\end{aligned}
$$

Here, $B = f_{\mathrm{mod,max}}$ denotes the effective measurement bandwidth. In the limit where $B \gg \frac{f_0}{2Q}$, the minimum detectable force gradient limited by thermal noise is given by

$$
\frac{\partial F}{\partial z} = \frac{2k}{f_0} \sqrt{\langle \Delta f_{\mathrm{th}}^2 \rangle} = \sqrt{\frac{4kk_B TB}{\pi Q f_0 A^2}}. \qquad (1.47)
$$

This expression defines the ultimate thermal noise floor of the AFM system.

1.2.6 Quartz Sensors

The qPlus sensor, largely pioneered by Franz J. Giessibl,[13,16] has become a cornerstone of modern AFM. It has evolved into a robust and widely adopted technique for high-resolution AFM studies that go beyond routine topographic or thin-film characterization. The qPlus design employs a quartz cantilever carrying a metallic tip, allowing simultaneous STM and AFM functionality. Its defining advantage lies in the exceptionally high stiffness of the cantilever, typically exceeding 1,000 N/m, which enables stable oscillation amplitudes on the order of a few ångströms and minimizes snap-to-contact instabilities. Furthermore, the qPlus configuration allows the use of conventional STM tips, often electrochemically etched tungsten, as the AFM probe. This compatibility facilitates the preparation of ultra-sharp tips, to which small molecules such as carbon monoxide can be attached, enhancing spatial resolution and chemical sensitivity. As a result, atomic-resolution imaging has become reproducible across many research groups,[6,17,18] even on insulating or weakly conducting materials that are inaccessible to traditional STM.

1.2.7 Horizontal vs. Vertical Probes

Most AFM experiments are conducted in the *horizontal geometry*, where the cantilever lies approximately parallel to the sample surface and the tip points vertically toward the sample. This configuration offers several practical advantages. First, it provides high spatial resolution since the dominant cantilever motion is purely vertical, making it highly sensitive to normal (out-of-plane) forces. Second, it enables direct measurement of vertical force gradients and simplifies optical alignment, as the geometry is well suited to conventional beam deflection or interferometric detection schemes. Additionally, the horizontal configuration integrates easily with cryogenic high-magnetic-field setups, where instrument dimensions are constrained by the radial bore of superconducting magnets.

An alternative approach, known as the *vertical* or *pendulum geometry*,[19] positions the cantilever perpendicular to the sample surface, such that its oscillation occurs parallel to the plane of the sample. This geometry allows direct probing of lateral or frictional forces as well as vertical forces and is particularly advantageous for studying in-plane phenomena, such as vortex pinning in superconductors or surface charge dissipation processes. It is also well suited to dissipation measurements, including Joule heating, because the lateral oscillation moves a localized charge puddle back and forth across the surface with constant amplitude, unlike in the horizontal geometry, where the charge distribution expands and contracts during oscillation. Furthermore, the pendulum configuration permits the use of very soft cantilevers, as the risk of snap-to-contact is greatly reduced compared to vertical-force geometries. This combination of stability and sensitivity makes the pendulum AFM geometry a powerful tool for quantitative studies of weak dissipative and lateral interactions in quantum materials.

1.2.8 Dissipative interactions in AFM

AFM is most frequently employed to measure the interaction forces between the tip and the sample, whether in contact or non-contact operation. As discussed in previous sections, FM-AFM possesses a second detection channel, the drive signal amplitude, that enables the measurement of non-conservative forces manifesting as energy dissipation. These dissipative interactions arise from various microscopic mechanisms, including van der Waals friction, electrostatic (Joule) losses, charge fluctuations, and phonon excitation, as illustrated in Fig. 1.8. Each of these processes represents a distinct physical channel through which energy is lost from the oscillating cantilever to the sample.

In practice, Joule dissipation is widely used to study local electronic and structural transitions, such as metal–insulator[20] or superconducting phase transitions[21]. Similarly, dissipative signatures arising from tunneling processes, such as charge trapping or localized ring tunneling in semiconductor, can be probed using the same detection channel[22]. Consequently, dissipation mapping in AFM provides a powerful and versatile means to probe both classical dissipative processes and quantum mechanical phenomena at the nanoscale.

For Joule dissipation in the horizontal geometry, the energy loss mechanism can be modeled by treating the tip–sample junction as a time-varying capacitor. As the cantilever oscillates, the capacitance changes in time, generating a displacement current $D(t)$ that depends on the applied bias U:

$$D(t) = \frac{\partial C}{\partial t} U = \frac{\partial C}{\partial z}\frac{\partial z}{\partial t} U. \tag{1.48}$$

Here, C is the tip–sample capacitance that varies with the instantaneous tip position $z(t)$, and $\dot{z}(t) = A\omega \sin(\omega t)$ describes the oscillatory motion of the cantilever with amplitude A and angular frequency ω. When the tip–sample circuit includes a finite resistance R_{ts}, Ohmic losses lead to Joule heating described by

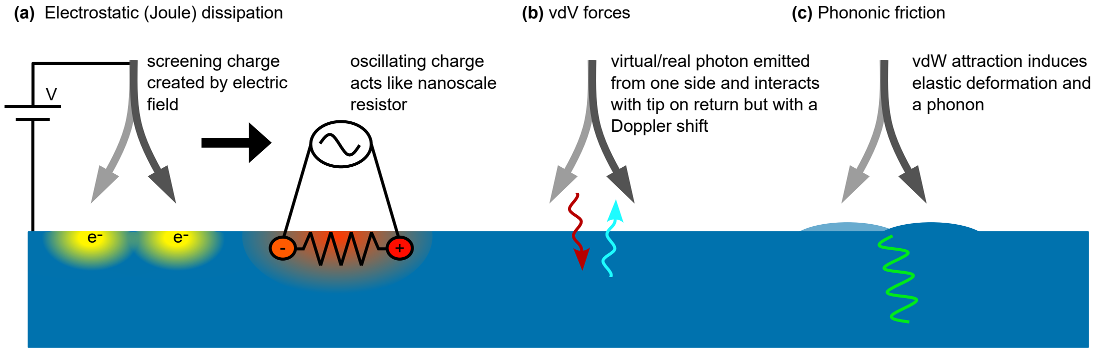

Figure 1.8: Schematic illustration of microscopic dissipation mechanisms in AFM. **(a)** Electrostatic (Joule) dissipation: oscillating tip-induced charges on the surface lead to displacement currents and resistive Joule losses. **(b)** van der Waals (vdW) friction: motion of the tip induces Doppler-shifted electromagnetic interactions between virtual or real photons, enabling energy loss through retardation effects. **(c)** Phononic friction: surface deformation induced by the tip motion generates phonon emission, carrying energy away from the tip–sample junction. Each process contributes to the non-conservative force component observed in the amplitude channel of FM-AFM.

$$P_{\text{Joule}} = TD^2(t) = R_{\text{ts}} \frac{\partial C^2}{\partial t} U^2 A^2 \omega^2 \sin^2(\omega t). \tag{1.49}$$

Averaging over one oscillation cycle gives the mean dissipated power,

$$\langle P_{\text{Joule}} \rangle = \int_0^{2\pi/\omega} P_{\text{Joule}}\, dt = \pi R_{\text{ts}} \frac{\partial C^2}{\partial t} U^2 A^2 \omega^2 \sin^2(\omega t). \tag{1.50}$$

which scales quadratically with both the applied bias and oscillation amplitude. This framework provides a quantitative link between the measured amplitude damping in FM-AFM and the local electronic dissipation processes within the sample.

In the pendulum geometry, we assume that the vertical change in the cantilever position is negligible and so the tip sample capacitance remains the same. In this case, the volume of the electron puddle below the cantilever from the electric field screening, V, should remain the constant through the oscillation. The instanenous current is written as

$$I(t) = \int \rho_{charge} * v(t) \tag{1.51}$$

where $\rho_{charge} = \frac{Q_{charge}}{V}$ and $v(t) = A\omega \sin(\omega t)$. Then the power can be written, given the local resistivity $\rho = R\frac{d_1 * d_2}{A}$ (d_1 and d_2 define the effective local surface area, width and depth respectively, of the charge perpendicular to the motion), as

$$P(t) = I(t)^2 R(2) = \rho \frac{A^2}{Vd_1}(QA\omega cos(\omega t))^2 \tag{1.52}$$

Given that $Q = VC$, the average power per oscillation cycle can be written as

$$\langle P \rangle = A^3 U^2 \rho \frac{(Cw)^2}{2Vd_1} \tag{1.53}$$

The power dissipation in the vertical geometry follows a square dependence on the applied bias and a cubic dependence on the amplitude of the oscillation. For a blunt tip, $C \sim \frac{1}{z}$, indicating a square dependence on the tip-sample distance. A more rigorous approach estimates $C \sim ln(1 + \frac{R}{z})$ where R is the radius of the tip.

We can also define a minimum threshold for dissipation in the cantilever based on its own intrinsic dissipation. All cantilevers will intrinsically dissipate energy. In the linear simple pendulum approach, we can write the equations of motion for the cantilever as

$$m_{\text{eff}} \frac{d^2 x(t)}{dt^2} + \Gamma \frac{dx(t)}{dt} + m_{\text{eff}} \omega_0^2 x(t) = f_{\text{ext}}(t) + F'(x(t)). \tag{1.54}$$

$f_{\text{ext}}(t)$ is the driving force acting on the cantilever to compensate for the energy loss due to dissipation and $F(x(t))$ is the force between tip and sample. The damping coefficient yields the frictional force through Stokes relation

$$F_{\text{friction}} = -\Gamma v. \tag{1.55}$$

Where Γ is the contribution of all dissipative channels such that

$$\Gamma = \sum_{0}^{N} \Gamma = \Gamma_0 + \Gamma_1 + \cdots + \Gamma_N. \tag{1.56}$$

Where $\Gamma_0 = \frac{k}{\omega_0 Q_0}$ for the intrinsic damping. The dissipated power of the free cantilever is then

$$P_0 = \frac{\pi k A^2}{e Q_0}. \tag{1.57}$$

Below this threshold, it is not possible to detect dissipation from other inelastic interactions between the tip and the sample.

2

Nanoscale Conducting and Insulating Domains on YbB_6

f-STATE ELECTRONS HAVE GENERATED SIGNIFICANT INTEREST IN QUANTUM MATERIALS DUE TO THEIR STRONG ELECTRONIC CORRELATIONS AND SPATIAL LOCALIZATION, WHICH CAN GIVE RISE TO A RANGE OF EMERGENT QUANTUM PHENOMENA. WITHIN THE HEXABORIDE FAM-

ILY, *f*-ELECTRONS HAVE BEEN SHOWN TO DRIVE MAGNETISM, NON-TRIVIAL BAND TOPOLOGY, AND KONDO HYBRIDIZATION EFFECTS. BEYOND THE *f*-ELECTRON SYSTEMS, OTHER HEXABORIDES EXHIBIT A VARIETY OF INTRIGUING PROPERTIES, INCLUDING ANTIFERROMAGNETIC ORDER, EXCEPTIONALLY LOW WORK FUNCTIONS, AND SUPERCONDUCTIVITY.[23] THE HEXABORIDE FAMILY THEREFORE PRESENTS A RICH PLATFORM FOR EXPLORATION, AS INTERFACING THESE MATERIALS OFFERS THE POTENTIAL TO ENGINEER NEW QUANTUM STATES, SUCH AS TOPOLOGICAL SUPERCONDUCTIVITY, THAT MAY HOST MAJORANA QUASIPARTICLES, PROVIDING A PROMISING AVENUE TOWARD QUANTUM COMPUTATION.

Rare-earth hexaborides host a diverse set of exotic properties, ranging from superconductivity to magnetism to non-trivial topology. Interest in hexaborides surged when SmB_6 was predicted to be the first of a new type of correlated electron system, termed a topological Kondo insulator (TKI), in which protected surface states span a Kondo gap pinned around the Fermi level (E_F)[24,25]. Extensive experiments, including transport[26,27,28,29,30,31,32,33], angle-resolved photoemission spectroscopy (ARPES)[34,35,36,37,38,39,40,41] and STM/STS[42,43], demonstrated the existence of two-dimensional metallic surface states on SmB_6 at low temperatures. However, the topological nature of these states was initially unclear due to the multiple atomic terminations with complicated polar structure[38,42,43,44]. Recently, quasiparticle interference (QPI) measurements on homogeneous terminations of SmB_6 revealed the heavy Dirac surface states within the Kondo gap[45,44], establishing SmB_6 as the first TKI.

YbB_6, a second TKI candidate, was predicted to host a mixed valence charge around $+2.2$ for Yb, inverted Yb $4f$ and $5d$ bands, and topological surface states similar to SmB_6[46]. Indeed, ARPES studies showed an odd number of Fermi pockets on the (001) cleaved surface of YbB_6[47,48,49,50], with the chirality of orbital angular momentum[47], spin texture[48], and temperature and photon energy dependence[49] expected for topological surface states. Quantum oscillation measurements confirmed consistent surface Fermi pocket areas[51,52]. However, magnetic susceptibility[53], optical reflectivity[54], and x-ray and ultraviolet photoemission[55] showed that Yb is uniformly divalent in the bulk of YbB_6, with a modest Yb^{3+} fraction only at the surface. Furthermore, the highest occupied Yb 4*f* state was consistently found around 1 eV below E_F[55,47,48,50,49], ruling out the TKI scenario, and requiring an alternate explanation for the surface states.

Two additional mechanisms for the YbB_6 surface states have been proposed. The first claims strong topological surface states originating from inversion of the bulk Yb 5*d* and B 2*p* bands[49,56], as schematized in Fig. 2.1(a). The second claims trivial quantum well states (QWS) due to band-bending at the polar (001) surface of YbB_6[57,58], as schematized in Fig. 2.1(b). The latter proposal is supported by the parabolic dispersion of (001) surface states[50], and additional ARPES measurements on the non-polar (110) surface showing a robust $\sim$ 0.3 eV gap between the B 2*p* valence and Yb 5*d* conduction bands[57]. Each proposal is supported by density functional theory (DFT) calculations with minor parameter variations. However, neither proposal appears fully consistent with all experimental data. All ARPES and quantum oscillation experiments on both (001) and (110) surfaces showed conducting states, despite the various *p*-type, *n*-type, and non-polar terminations expected. Yet no surface channel was seen in magnetoresistance measurements[30]. Given the likelihood of spectral artifacts from these existing experiments that spatially average over different terminations[44], it remains crucial to conduct local imaging experiments to distinguish between proposals by spatially correlating surface spectral features with specific terminations.

Here, we use STM/STS to demonstrate termination-dependent surface conductivity in YbB_6. Our spatially-resolved differential conductance spectra (dI/dV) show strong band bending associated with surface polarity, leading to coexisting insulating and conducting domains. The observation of insulating domains on clean regions of YbB_6 definitively rules out the possibility of a strong topological insulator state. Within the conducting domains, we observe multiple in-gap peaks reminiscent of van Hove singularities (VHS) that may stem from Rashba spin-split QWS, schematized in Fig. 2.1(c).

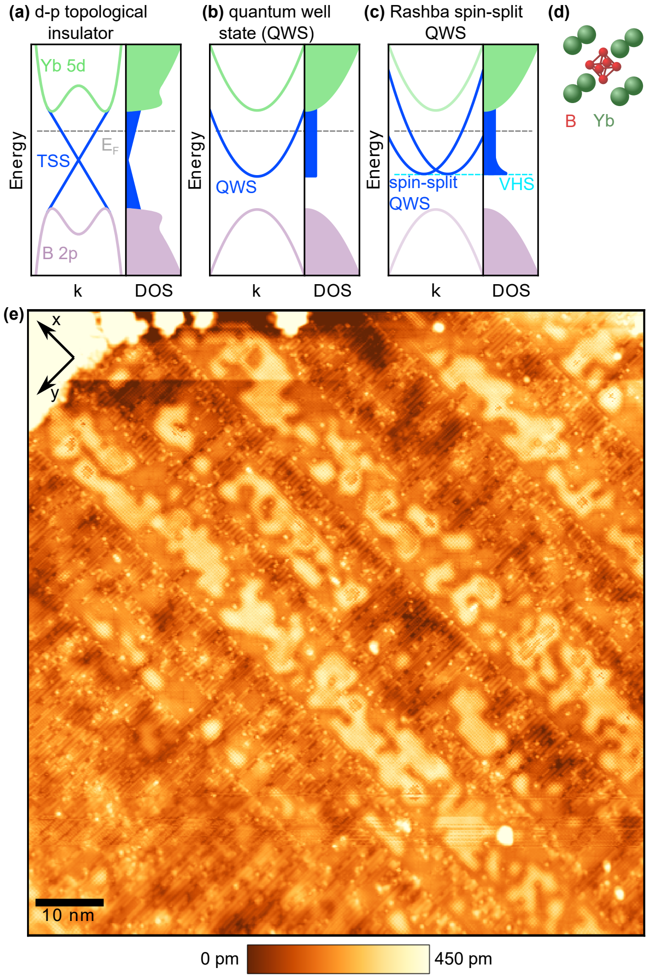

Figure 2.1: Three proposals for YbB_6 electronic band structure and associated density of states (DOS): **(a)** Topological surface state (TSS), **(b)** quantum well state (QWS), and **(c)** Rashba spin-split QWS. See additional details in Fig. 4.1 in the Appendix, section 4.1. **(d)** CsCl crystal structure of YbB_6. (e) STM topographic image, showing multiple terminations on cleaved YbB_6 (sample bias $V_s = -0.15$ V; setpoint current I_s = 100 pA). Values on the color bar indicate apparent height and not actual height, due to the polar surface effects in YbB_6.

2.1 Atomically-resolved topographic map

A single crystal of YbB_6 was grown by the Al-flux method[30], cleaved in ultra-high vacuum (UHV) at cryogenic temperature, and immediately inserted into a home-built STM at 4.2 K. YbB_6, possessing a CsCl-type crystal structure shown in Fig. 2.1(d), does not have a natural cleavage plane. Because the intra- and inter-octahedral B-B bonds have similar lengths[61], several terminations are possible by breaking both types of bonds. Breaking inter-octahedral bonds results in the B_6 and Yb terminations. Alternatively, breaking intra-octahedral bonds can lead to disordered and inhomogeneous terminations with incomplete B octahedra. In our STM study, we find the surface morphology of cleaved YbB_6 exhibits both 1×1 and chain-terminated surfaces, arranged in alternating strips along the [100] crystal axis, as shown in Fig. 2.1(e). On the 1×1 terminations [Fig. 2.2(a,c)], we measured an atomic spacing consistent with the expected YbB_6 lattice constant of $a = 4.1439$ Å[61,62,63]. On the chain terminations [Fig. 2.2(b,d)], the inter-chain period is exactly doubled.

2.2 *dI/dV* ANALYSIS AND SURFACE IDENTIFICATION

Average *dI/dV* spectra, representing the local density of states (DOS), from each termination are shown in Fig. 2.2(e). Both spectra exhibit a large range of reduced DOS around E_F, and prominent peaks at negative bias, which we identify as the Yb^{2+} 4*f* multiplets. These 4*f* states are often observed by spatially-averaged ARPES experiments around -1 eV and -2.3 eV[47,48,49,50], though energies may vary by up to 500 meV between samples[47] and time after cleaving[50]. The chain termination spectra exhibit an additional rise at positive bias, which may be identified as a broad Yb 5*d* band, as observed by inverse photoemission[54]. The energy shift between our *dI/dV* spectra suggests terminations with different surface polarities, as commonly observed via spatially-resolved measurements on other semiconductors[64,44]. On cleaved YbB_6, we expect that a Yb-terminated surface would be positively charged compared to the bulk because the B octahedra take electrons from the Yb layer to form their bonds. Bulk free electrons then move towards the surface to screen the positive surface electrostatic potential, forming an accumulation layer with excess electrons (*n*-type), and inducing a downward band-bending. Similarly, we expect that a B_6-terminated surface would be negatively charged, giving rise to a p-type environment and upward band-bending. However, not all B-terminated surfaces need be negatively charged; e.g., the B_1 termination requires fewer electrons from the Yb layers to form the octahedral bonds.

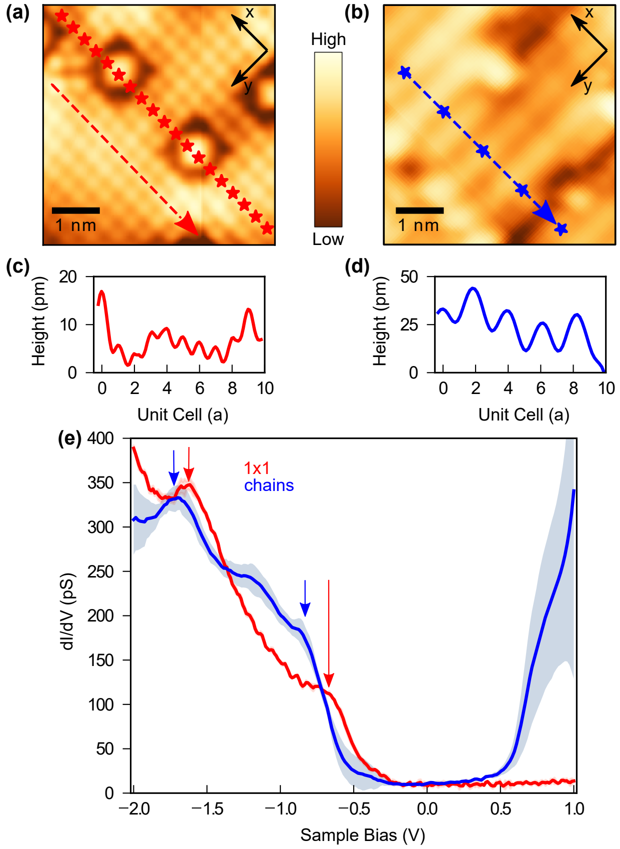

Figure 2.2: (a, b) High resolution topographies of YbB_6 (001) surface showing two distinct terminations: (a) 1×1 (V_s = -0.4 V, I_s = 200 pA) and (b) chain (V_s = 0.2 V, I_s = 100 pA). **(c, d)** Linecuts along respective dashed lines, calibrated to the YbB_6 lattice constant $a = 4.1439$ Å[61,62,63]. **(e)** *dI/dV* spectra averaged over the starred locations in (a) and (b), with shaded standard deviation (V_s = -2 V, I_s = 400 pA, lockin modulation V_{rms} = 10.6 mV). Vertical arrows point to Yb^{2+} $4f$ multiplets, shifted by surface band bending between the two terminations.

In the dI/dV spectra of Fig. 2.2(e), the low-conductance energy range around E_F on the chain termination is smaller than that on the 1×1 termination. The change in energy range can be explained by a combination of tip-induced band bending (TIBB), polar surface band bending, and the presence of in-gap surface states. STM measurements of insulator gap amplitudes are known to vary from their intrinsic values as a result of poor electronic screening, which allows the electric field generated by the tip to partially penetrate the sample surface[65]. For semiconductors with polar surfaces, tip-induced bending of the bulk bands at the surface can lead to apparent variations in gap amplitude and shifts of the gap between different surfaces[64]. YbB_6 is subject to both band-bending effects, in addition to in-gap states that can alter the electronic screening and thus the overall energy separation.

Combining topographic and spectroscopic data, we can identify the two observed terminations. The upward band shift on the 1×1 termination tells us that it must possess a greater number of negatively-charged B atoms with respect to the chain termination, so it cannot represent a Yb termination. Due to its clean structure and atomic periodicity, we infer that the 1×1 termination is either B_1 or B_6. In contrast, the double periodicity of the chains tells us that it is a partial layer termination. Furthermore, the chains are laterally offset from the 1×1 atoms, as highlighted in Fig. 2.3(a), where blue lines indicate the chain centers and red dots indicate the top B atoms of each octahedron. Averaged linecuts for the chain and 1×1 terminations are shown in Fig. 2.3(b). We can therefore rule out a partial Yb termination as the chain identity, because Yb chains would lie directly between 1×1 B_1 or B_6 surface atoms. Therefore, the chains can be identified as a partial B termination. Due to the up-shifted (*p*-type) spectra, we know that the 1×1 termination must have more B atoms than the chain termination, so we conclude that the 1×1 termination must be B_6 rather than B_1. The proposed structure of the 1×1 termination and an example B_4 chain termination for the chain domain are illustrated in Fig. 2.3(c,d), respectively. Other possibilities for the chain termination include B_2, B_3, tilted B_5, or tilted B_6 octahedra (Fig. 4.2 in the Appendix, section 4.2).

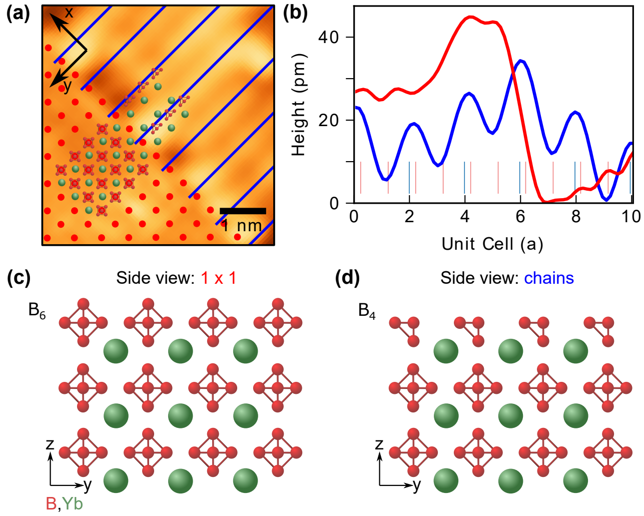

Figure 2.3: (a) Topography showing a boundary between 1 × 1 and chain terminations (V_s = 0.2 V, I_s = 100 pA). The blue lines are along the centers of the chains and the red points correspond to the individual atoms on the 1×1 surface. **(b)** Averaged linecuts across 1×1 and chain terminations in (a). Vertical lines represent the unit cell spacing for each surface. **(c, d)** Side view of the B_6 and B_4 surface terminations, respectively. For a more complete set of possible chain terminations, see Fig. 4.2 in the Appendix, section 4.2

2.3 DETERMATION OF SURFACE STATE

To understand the YbB_6 surface states previously observed by spatially-averaging probes[47,48,49,50,51,52], we zoom in on the near-E_F states that are swamped by the dominant 4*f* multiplets in Fig. 2.2(e). Figure 2.4 shows the analysis of a topography and *dI/dV* map, acquired over a smaller energy range around E_F, with lower junction resistance for increased sensitivity to sub-gap features. With this increased sensitivity, we observe a true insulating gap on ∼25% of the surface, corresponding to clean regions of the 1×1 termination in Fig. 2.4(a), and depicted in a black-red colorscale in Fig. 2.4(b). The average spectra from these insulating domains are shown in corresponding colors in Fig. 2.4(c), with apparent gap amplitude ∼100 meV roughly consistent with the known bulk gap[53]. We caution that TIBB is likely more significant at this lower junction resistance, where the tip is closer to the sample, but we emphasize that TIBB cannot create an apparent gap, though it can change an

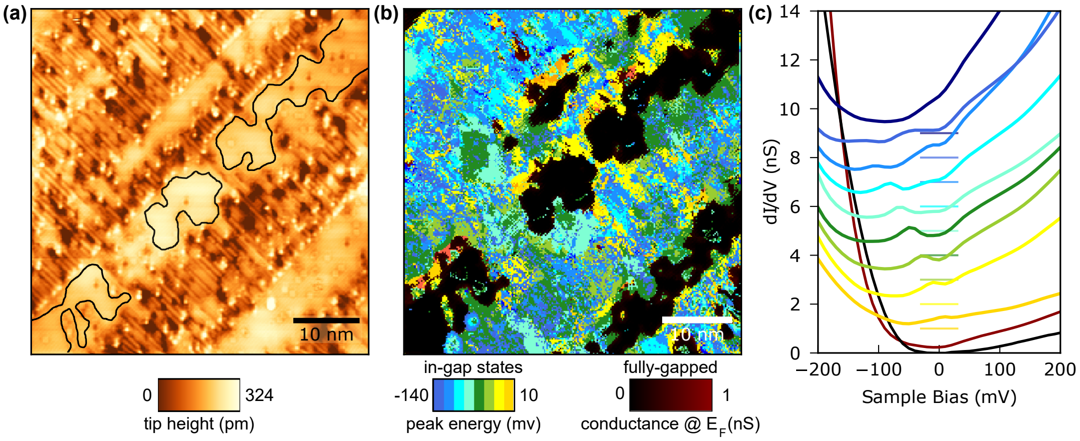

Figure 2.4: **(a)** Surface topography (V_s = -1 V, I_s = 50 pA). **(b)** Map showing the presence (bright colors) or absence (dark colors) of in-gap states, analyzed from a *dI/dV* map acquired in the same area as (a) (V_s = -0.2 V, I_s = 200 pA, V_{rms} = 10.6 mV). For each *dI/dV* spectrum in this area *with* in-gap states (average $>$ 1 nS from -20 meV to $+20$ meV), we depict the *energy* of the first in-gap peak (if any) above the valence band edge in a rainbow palette. Less than 1% of the surface exhibits substantial in-gap spectral weight without discernible peak; these few pixels are depicted in dark blue. Areas *without* in-gap states (average $<$ 1 nS from -20 meV to $+20$ meV) are shown instead using a black-red palette depicting this average tunneling *conductance* near E_F. Outlines of several large insulating domains in (b) are superimposed on (a) for direct comparison to atomic termination. **(c)** Averaged *dI/dV* spectra based on the binning in (b) show sub-gap peaks in the 8 color bins, each offset vertically by 1 nS with horizontal lines to represent their zero for clearer comparison. Close to 25% of the surface spectra show no in-gap states. These gapped spectra, averaged over regions with tunneling conductance below 1 pS (black) and above 1 pS (dark red) are shown with zero offset, but $3\times$ magnification to emphasize the true Fermi-level gap.

existing gap amplitude. Therefore, the $\sim$25% gapped area definitively rules out a strong topological surface state, which would necessarily cover all surfaces[66,67].

The remaining $\sim$75% of the YbB_6 surface, comprising most of the chain termination and a smaller fraction of the 1×1 termination, shows in-gap states with one or two peaks at energies near E_F. The average spectra, binned by their minimum in-gap peak energy, are shown in Fig. 2.4(c). Though YbB_6 is a bulk insulator[53], the demonstrated surface polarity may bend a bulk band to cross E_F at the surface. Confinement within a few nanometers of the surface reduces the 3-dimensional band to a discrete number of 2-dimensional bands known as quantum well states (QWS), as suggested by previous ARPES experiments[50,57], and schematized in Fig. 2.1(b). But QWS alone would not give rise to peaks in the density of states. To explain our observed peaks, as well as the spin-polarization measured by ARPES[48], we suggest that Rashba spin-orbit coupling (SOC) splits the surface bands, as schematized in Fig. 2.1(c). Spin-splitting reconstructs the DOS, giving rise to a van Hove singularity and an observable peak in dI/dV at the minimum energy of each QWS band[64,68]. The $\sim$150 mV spatial variation of the sub-gap peak energies in Fig. 2.4(c) may be attributed to band bending from the two surface terminations, and more local band bending from the many atomic-scale defects apparent in Fig. 2.4(a). Schematics of variable surface band bending giving rise to one or two QWS, and spin-splitting giving rise to VHS peaks in the DOS, are shown in Fig. 4.1 in the Appendix, section 4.2. Another possible source of spatially-modulated peaks in the density of states – Friedel oscillations, or more generally quasiparticle interference arising from scattering off surface defects[69] – is not relevant in this case because high defect density destroys the coherence of scattered waves over most of the surface.

2.4 Conclusion

In conclusion, our STM/STS study provides the first real-space imaging of YbB_6. On the (001) surface, we observe two different atomic terminations whose distinct polarity is evidenced by spectral shifts greater than 100 meV. Furthermore, we observe both conducting and insulating nanoscale domains, definitively ruling out the proposed strong topological surface state for YbB_6. Instead, we show that the surface states previously observed by spatially-averaging techniques arise from QWS induced by surface band bending. Throughout these conducting domains, we find sub-gap peaks consistent with VHS arising from Rashba spin-splitting of the QWS. The coexisting nanoscale domains and terminations with differing surface polarities suggest YbB_6 may represent a new class of strongly-correlated materials with utility for spin-polarized *p-n* junctions or other spintronic devices[64]. Spin-polarized STM could be an important tool to confirm, quantify, and possibly manipulate the spin-polarization of the nanoscale surface domains.

3

Design of a modular millikelvin scanning probe microscope for characterizing and manipulating quantum materials and devices

ULTRA-LOW TEMPERATURES UNLOCK ACCESS TO FRAGILE QUANTUM PHENOMENA THAT CAN ONLY EXIST WHEN THERMAL EXCITATIONS ARE SUFFICIENTLY SUPPRESSED. Examples include Majorana bound states in topological superconductors[3,70,71,72], the competing magnetic-order and Kondo interactions in topological surface states,[31] and interaction-driven superconductivity in twisted van der Waals heterostructures.[73,74] The focus of condensed matter physics has broadened from bulk single crystals to engineered, low-dimensional platforms and device architectures such as kagome metals, quantum-confined superconducting films, moiré materials, quantum dots, and Josephson junctions. STM has played a central role in advancing these frontiers by visualizing correlated flat bands in twisted heterostructures,[75] charge order in kagome lattices,[76] and vortex-bound states in iron-based superconductors.[3] Yet many experiments remain constrained by operating temperatures above the relevant energy scales, the need for specialized tip preparation (e.g., spin-polarized[72,77,78]), and the challenges of preparing exfoliated heterostructures or microfabricated devices for STM access.

Millikelvin temperatures are also essential for studying quantum materials because only at such low energies are classical thermal fluctuations fully frozen out, allowing intrinsic quantum fluctuations and dissipation processes to dominate. In this regime, emergent electronic and magnetic behaviors, such as unconventional superconductivity[79], topological edge conduction[31], and Majorana coherence[3,70,71,72], arise purely from quantum mechanical interactions. Dissipation measurements at millikelvin temperatures provide a direct probe of the fluctuation–dissipation dynamics that govern these states, revealing how quasiparticles, phonons, and defects exchange energy at the atomic scale. By operating below 100 mK, one can disentangle conservative and dissipative forces, resolve microscopic energy-loss channels, and quantify the limits of coherence and stability in correlated quantum systems.

Realizing STM and dissipative AFM measurements at millikelvin temperatures imposes stringent design requirements on the microscope and cryogenic system. SPMs designed for quantum devices must accommodate a high density of electrical contacts to apply gate voltages or transport currents through mesoscopic structures. They also require reliable coarse navigation over millimeter-scale distances to locate exfoliated flakes or lithographically defined regions and to access auxiliary surfaces for tip conditioning. Capacitive position sensing is essential for accurate relocation between these regions. For the highest level of dissipation sensativity, ultra-soft silicon cantilevers are needed, requiring the use of optical readout in an exceptionally minimal power cooling environment. At the same time, the microscope head must maintain exceptional mechanical rigidity and isolation from both cryogenic and environmental vibrations. Finally, as scanning probe methods continue to diversify, the instrument must remain modular and adaptable, capable of supporting future experimental configurations without a complete redesign.

In this work, we present the design and implementation of a modular millikelvin SPM optimized for quantum materials and device characterization. Our system integrates a compact two-stage vibration isolation assembly with an UHV dilution refrigerator (DR), achieving a base temperature of 63 mK. A shuttle-based microscope head provides dense electrical connectivity through BeCu side contacts while reserving shielded connectors for low-noise measurement lines. Integrated capacitive sensing and three-axis coarse positioning motors allow reliable navigation between samples, devices, flakes, and tip-preparation sites. The SPM is capable of performing STM and AFM with the AFM implementation accomplished through the use of both qPlus based sensing, enabling sub-atomic resolution owing to the cantilever stiffness, and silicon based cantilevers enabling highly sensative force and dissipation measurements. To ensure low electron temperatures, we incorporate cartridge-style powder filters whose transmission and reflection characteristics are characterized up to 67 GHz. Together, these components yield a versatile platform that achieves requirements of modern SPM studies. In the following sections, we describe the vibration isolation system, cryogenic and vacuum architecture, microscope head design, powder filter performance, and measured tunneling spectra.

3.1 VIBRATION AND ACOUSTIC ISOLATION

We implement a two-stage vibration isolation system consisting of pneumatic isolators for the first stage (weighing $\sim$ 15.5 tons) and elastomer dampers for the second stage (weighing $\sim$ 1,200 lbs) to suppress low-frequency building resonances. Two-stage pneumatic systems are common in state-of-the-art STMs, but they are typically bulky and expensive. To achieve comparable isolation performance within a compact footprint and avoid the resonance enhancement caused by stacked pneumatic stages,[80] we constructed a “room-within-a-room” structure (Fig. 3.1(a)) that provides two layers of acoustic and vibrational isolation. Both rooms are mounted on rubber pads to minimize coupling to the building foundation. Inside the inner room, a passively floated floor supported by pneumatic isolators (Fig. 3.1(b)) provides the primary low-frequency isolation.[81]

To further reduce coupling to building resonances and to address the limited ceiling height of our facility, a second isolation stage was implemented directly beneath the microscope using elastomer dampers[82] combined with a lead-shot–loaded wooden support table (Fig. 3.1(c)). Elastomer damping elements, while less common in STM installations, were selected for their compact form factor (additional information provided in the Appendix, section 4.3.1) and their ability to dissipate mid-frequency vibrations that would otherwise be amplified in a stacked pneumatic design. Auxiliary mechanical components, including a gimbal isolator for lateral alignment (Fig. 3.1(d)) and damped bellows connectors to decouple acoustic transmission along the pumping lines (Fig. 3.1(e)), further suppress residual vibrational coupling between the cryostat and gas-handling system. In Fig. 3.1(f), the single stage, stacked pneumatic stages, and stacked elastomer stage transmissibility are plotted in the low frequency range. While stacked pneumatic isolators offer superior performance at higher frequencies, their effectiveness at low frequencies, relevant to typical building vibrations is reduced. In contrast, the stacked elastomer design maintains low-frequency performance comparable to a single-stage system while enhancing damping at higher frequencies.

3.2 ULTRA HIGH VACUUM CHAMBERS AND CRYOGENIC EQUIPMENT

The cryogenic system consists of a liquid helium dewar integrated with a 14 T superconducting magnet[84] (Fig. 3.2(a)). The dewar is supported by four stainless-steel legs that rest on the wooden isolation table described in the Appendix, section 4.3.1, providing both mechanical stability and vibrational damping. A DR[85] is mounted to the top of the dewar, and the combined cryostat assembly is mechanically decoupled from the surrounding UHV chambers by a flexible stainless-steel bellows. With the DR installed, the liquid helium capacity is approximately 150 L, providing a hold time of roughly 10 days before the helium level falls below the operational threshold for DR circulation. The magnet is a single-axis superconducting solenoid operating in persistent mode, with

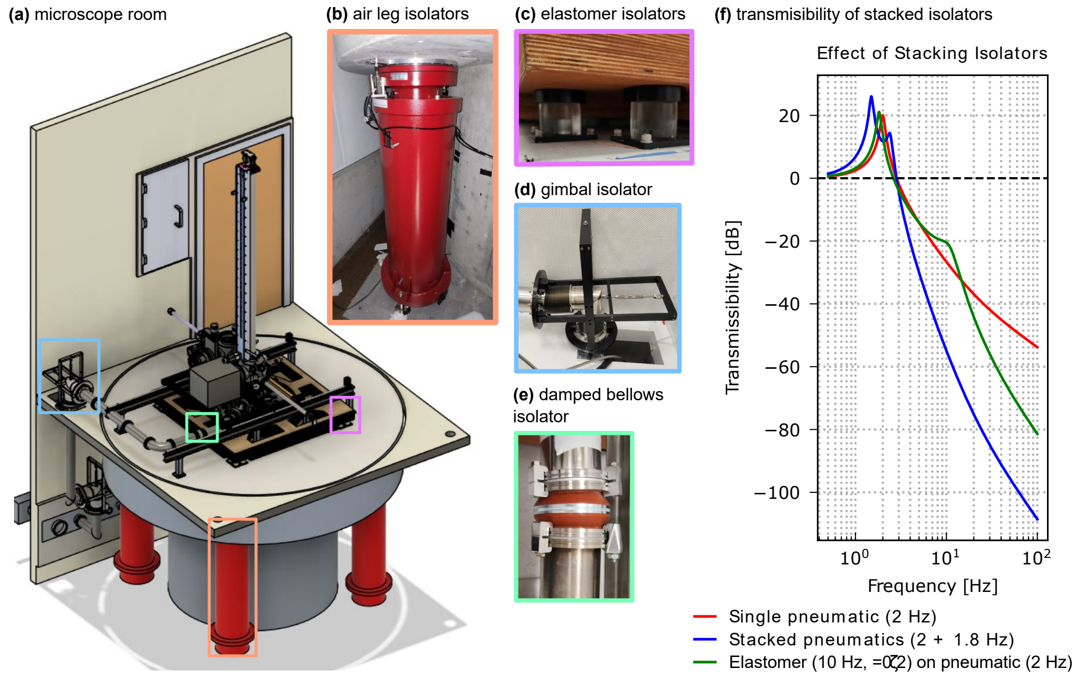

Figure 3.1: (a) Cross-sectional view of the microscope room showing the nested "room-within-a-room" construction for acoustic and vibrational isolation. **(b)** Primary air-leg pneumatic isolators[83] that support the floating inner floor. **(c)** Second-stage elastomer isolators combined with a lead-shot–loaded wooden table to absorb mid-frequency vibrations. **(d)** Gimbal isolator used for lateral decoupling of the support frame. **(e)** Damped bellows isolator that suppresses acoustic transmission along pumping lines. **(f)** Modeled transmissibility curves comparing different isolation configurations: a single pneumatic isolator (red), stacked pneumatic isolators (blue), and elastomer isolators mounted on pneumatics (green). The combined pneumatic–elastomer design provides enhanced attenuation above 10 Hz while avoiding large amplification at low-frequency resonances.

a drift rate of $\leq$10 ppm/hr. To mitigate magnetic interference with neighboring laboratories, the magnet is equipped with an active stray-field cancellation system. This reduces lateral fringe fields at full 14 T operation to below 0.007 G at a distance of 5 m and 0.005 G at 10 m, ensuring stable high-field performance without perturbing nearby instruments.

The UHV DR (shown in Fig. 3.2(a)) enables cooling to millikelvin temperatures and is configured with additional provisions for radio-frequency (RF) filtering and cryogenic signal amplification. Specifically, the mixing chamber includes custom RF filter mounts and mouting for the dock-

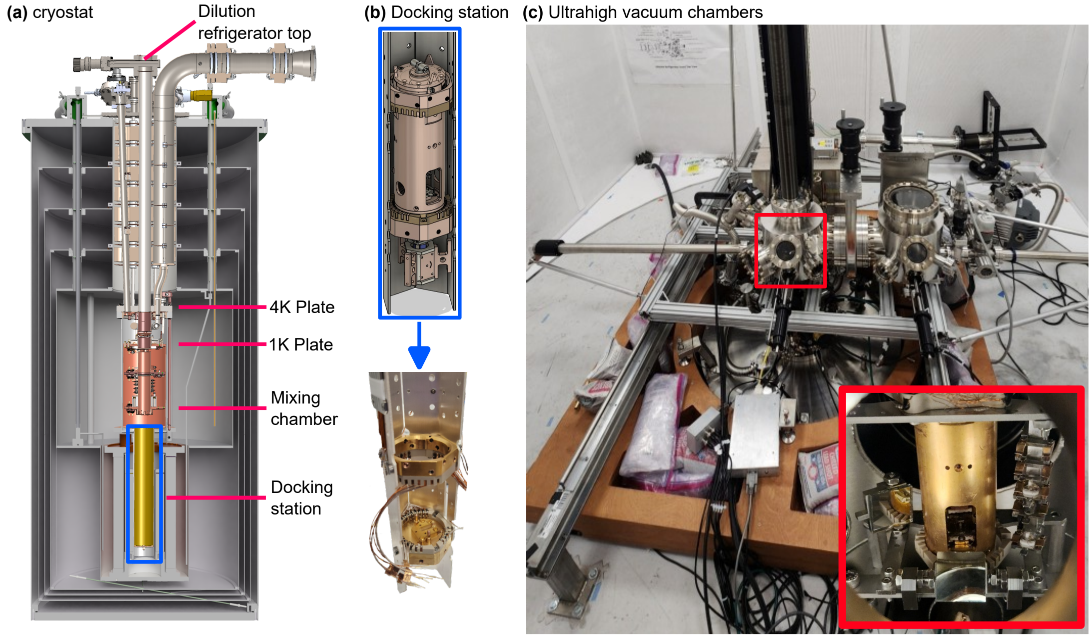

Figure 3.2: (a) Cutaway schematic of the integrated cryogenic system showing the 14 T superconducting magnet and liquid helium dewar. The dewar supports the DR while being mechanically isolated from the surrounding UHV chambers by a bellows. The 4 K plate, still, heat exchangers, and mixing chamber are labelled. **(b)** CAD model and photo of the docking station with the shuttle included in the former. **(c)** Photo of the UHV chambers where probes and samples are inserted, prepared, stored, and loaded into the microscope. Inset shows a photo of the inside of the central chamber where the SPM shuttle hangs in the middle for probe or sample exchange.

ing station of the SPM (Fig. 3.2(b), while the 4 K stage houses a cryogenic preamplifier for low-noise signal detection. The DR employs a multistage cooling sequence to precool and liquefy the circulating helium mixture before entering the mixing chamber, where the dilution process occurs. The sequence begins with precooling via submerged tubing in the 4 K liquid helium bath, followed by a Joule–Thomson (JT) condensing unit that liquefies the ^{3}He component. The mixture then passes through a network of high-impedance capillaries, a still, and silver sinter heat exchangers that progressively thermalize and compress the gas before expansion. A JT condensing stage was chosen over a conventional 1 K pot to reduce mechanical vibration and electronic noise, albeit at the expense of reduced cooling power.

In the mixing chamber, the helium mixture separates into two phases: a concentrated ^{3}He phase and a dilute phase containing ^{3}He dissolved in ^{4}He (with a solubility limit of $\sim$6.6%). The cooling power arises as ^{3}He atoms cross the phase boundary from the concentrated phase into the dilute phase, absorbing energy in the process. The dilute mixture is continuously circulated through the still, where ^{3}He is preferentially evaporated due to its higher vapor pressure. This evaporation is enhanced by heating the still, which increases the ^{3}He flow rate and thereby the cooling power of the mixing chamber. The evaporated ^{3}He is subsequently purified through liquid-nitrogen traps and reintroduced into the circulation line.

The cooldown time from room temperature to the base temperature of 63 mK is approximately 71 hours: 36 hours from room temperature to 78 K; 24 hours from 78 K to 4 K; and 3 hours from 4 K to base temperature. Once stabilized, the temperature stability of the DR is better than 1 mK, providing the necessary conditions for high-resolution STM and AFM measurements at millikelvin temperatures.

The UHV chamber assembly provides optical access for probe and sample insertion, as well as *in-situ* preparation, storage, and alignment (Fig. 3.2c). Gate valves separate the three primary regions of the system: the load-lock chamber, where new samples and probes are introduced; the preparation chamber, where tips and samples can be cleaned or treated; and the central chamber, which serves as both a storage area and a docking interface for the shuttle during tip and sample exchange. The preparation and load-lock chambers are each equipped with dedicated turbomolecular pumps, while the central chamber is maintained by an ion pump in combination with a titanium sublimation pump. During microscope operation, the turbomolecular pumps are spun down to minimize vibration, and vacuum in both the central and preparation chambers is maintained by the ion pump. Following bakeout, the base pressure of the UHV system reaches $\leq 5 \times 10^{-10}$ torr.

The entire UHV assembly is mounted on a movable carriage that slides along a rail system, allowing the chamber set to be disconnected from the DR via the bellows interface and retracted for cryostat maintenance. This design choice was essential given the limited vertical clearance of the laboratory and provides convenient access to internal components without compromising vacuum integrity or alignment. It also allows for the plinth of the first isolation stage to be complete as the dewar does not need to be accessed from the bottom, thus pushing its natural resonance frequencies higher.

Wobble sticks are employed in both the preparation and central chambers for tip and sample manipulation. In the main chamber, the wobble stick enables transfer of sample and probe holders between the storage rack, transfer arm, and the motorized DR manipulator[86]. It also provides manual control for adjusting two alignment mirrors positioned at the front and side of the shuttle when docked within the UHV chamber. These mirrors direct light toward a camera–lens imaging system that monitors the relative position of the tip and sample, enabling optical localization of small targets such as exfoliated flakes and lithographically defined devices.

The electrical wiring of the scanning probe microscope is routed through dedicated lines that extend from the room-temperature feedthroughs to termination points inside the shuttle, as illustrated in Fig. 3.3. Powder filters are installed on all measurement-related lines to suppress high-frequency noise and reduce electron temperature, while non-measurement lines remain unfiltered since they do not contribute to thermal broadening. Electrical contact between the shuttle and docking station is achieved through BeCu fingerstock springs[87] that make uniform side contact with the shuttle. Each spring is individually soldered to a copper block and epoxied into a PEEK ring using Stycast 2850 FT with catalyst 23 LV. This side-contact design provides a larger area for electrical connections while preserving the bottom surface of the shuttle for high-priority tunneling-current lines, which use SMPM connectors and semi-rigid coaxial wiring to ensure effective shielding and minimize triboelectric noise. Twisted-pair wiring is used for temperature sensors, AFM channels, and capacitive measurement lines to suppress common-mode interference.

To avoid thermal shorting between the 4 K helium bath and the room-temperature upper stages

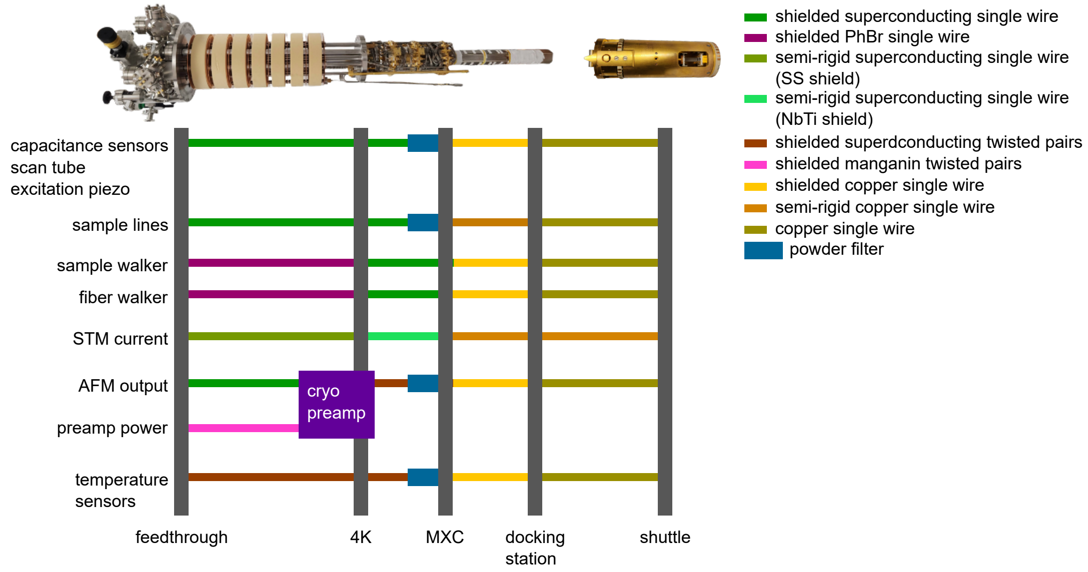

Figure 3.3: Wire selection prioritizes thermal insulation from room temperature to the mixing chamber stage by employing superconducting or phosphor bronze cabling. From the mixing chamber stage to the shuttle, copper cabling is used into maximizing heat sinking to the mixing chamber.

of the DR, superconducting cabling is used for all lines except the piezoelectric motor leads. The motor lines employ phosphor-bronze (PhBr) wire to maintain low resistance along the segments that do not remain superconducting between the 4 K stage and the room-temperature feedthroughs. All wiring is shielded continuously up to the docking station to minimize cross-coupling and electromagnetic interference. From the mixing chamber to the docking contacts, highly conductive copper wiring is employed on all lines to ensure optimal thermal anchoring and minimal voltage drop. Coaxial cables are used for non-measurement lines, while semi-rigid coax is reserved for sensitive measurement channels. The shields of all lines are grounded to the metallic body of the DR. The DR itself is electrically referenced to the SPM controller solely through the bias coax line connected at the feedthrough flange, providing a single-point grounding scheme to prevent ground loops. The wiring descending along the docking station is thermally anchored to the silver hexagonal body using stainless-steel clamps and secured in multiple locations with polytetrafluoroethylene

(PTFE) tape to maintain strain relief and thermal contact.

3.3 Scanning probe head design

At millikelvin temperatures, under UHV, and in large magnetic fields, careful material selection is critical to ensure compatible thermal contraction, efficient thermal conduction, and appropriate electrical properties. Our SPM design primarily employs gold-plated copper, silver, Macor, and PEEK. While thermally insulating materials are useful to connect the stages of the DR together, from the mixing chamber into the shuttle high thermal conductivity is needed along with matching thermal contraction in several key points. This limits many materials used in 1K-4K microscopes, mainly titanium, as many of these materials will superconduct or are too thermally insulating. To achieve high thermal conductivity, pure silver is used for the body of the docking station as this provides the greatest thermal conductivity of any metal. Copper is used for all wiring and provides the bulk of the cooling to the probe and the sample given copper's excellent thermal conduction. Additionally, we gold plate exposed copper as this limits oxidation and provides a better thermal contact over long periods. Macor as an electrical insulator is mainly used within the shuttle as the material provides greater thermal conductivity than PEEK and other plastics while being more machinable than its other ceramic counterparts such as Al_2O_3.

The SPM shuttle (Fig. 3.4a) requires a robust locking mechanism to couple securely to the manipulator and dock into the DR with both strong thermal contact and mechanical stability. The design (top of Fig. 3.4(b,c)) operates using a manipulator with only two degrees of freedom, enabling dependable transfer without requiring rotational alignment control. The connection between the manipulator and shuttle is achieved via a bayonet-style lock actuated by an inner rotating shaft. The bayonet key features an asymmetric base that pushes against a spring-loaded pin, moving the pin laterally as the key is rotated in either direction. This single-pin docking mechanism provides

Table 3.1: Preferred materials for use in a DR. Produced from data in Balint *et. al.*[88] unless indicated otherwise. Thermal conductivity (κ) is given for 4 K. Linear Expansion ($\partial L/L_{293}$) is listed for 293 K to 4 K. *Value listed for 293 K. **Value listed for 173 K. ***Value listed for 80 K, ****Value listed for 20 K.

Material	κ (W/m*K)	$\frac{\partial L}{L_{293}}$ (10^{-6})	Density (g/cm^3)
Copper (OFHC, RRR=500)	3182	-1915.62[89]	8.94
Silver	6000[90]	-3732.692[91]	10.49
Aluminum (6061)	5.3	-4138.46	2.7
Beryllium	****3000[90]	-1216.44	1.85
Beryllium Copper	1.88	-3131.19	8.25
Phosphor Bronze	4.64[89]	-3370.679[89]	8.85
Molybdenum	56.74	-913.79	10.22
Titanium	5.19[92]	-1581[92]	4.51*
Steel 316	0.272	-2169.85	8.0
Sapphire	148[93]	-789.37	4.0
Macor	*1.46[94]	**-1012.5[94]	2.52
Alumina	376[95]	-2058.298[96]	3.97
Aluminum Nitride	0.5[97]	***-298[97]	3.26
PEEK	0.012[98]	***234.742[99]	1.3

both thermal anchoring and mechanical rigidity, with actuation confined to one side for simplicity (Fig. 3.4c). The outer tube of the manipulator is mechanically constrained from rotation, ensuring that the shuttle remains rotationally locked during transfer. To guarantee proper alignment of the electrical contacts within the docking stage, two guide pins are mounted at the base of the docking station, engaging with the shuttle during the final 5 cm of insertion.

SPM systems require at minimum a coarse Z motor to approach the probe tip to the sample, and additional XY nanopositioning greatly enhances versatility by allowing motion between multiple devices, tip-preparation films, or sample regions. Our shuttle incorporates a stacked three-axis piezo walker (center of Fig. 3.4b) that combines shear-piezo stacks with capacitive sensing for submicron positioning accuracy. The Z walker employs a Pan-style geometry[100] with an 8 mm travel range, while the XY walker uses a plate-style design providing a hexagonal motion envelope with a 3 mm apothem. At base temperature, walker operation typically requires 260 V, maximizing range while

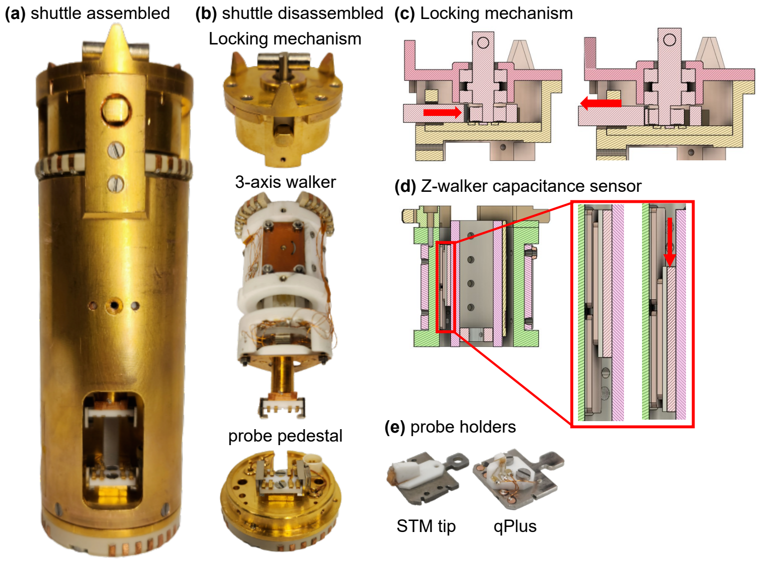

Figure 3.4: **(a)** Fully assembled microscope shuttle showing the gold-plated outer housing. **(b)** Shuttle disassembled into major components, including the locking mechanism, three-axis piezo walker, and probe pedestal. **(c)** Cross-sectional schematic of the single-pin locking mechanism, which secures the shuttle to the docking station and provides thermal anchoring. **(d)** Diagram of the Z-walker capacitive sensing assembly, with inset showing differential signal variation as the slider moves between electrodes. **(e)** Interchangeable probe holders designed for STM and qPlus AFM operation. Together, these components form a modular shuttle system that combines reliable docking, coarse nanopositioning, and high mechanical stability for millikelvin scanning probe measurements.

minimizing local heating. The shear stacks use a unique metal-to-sapphire interface featuring BeCu contact pads that glide against the sapphire slider. These BeCu pads are easier to polish than conventional Al_2O_3 surfaces and yield superior contact uniformity, improving motion stability and reducing wear over repeated cycles.

Capacitive sensing is integral for reproducible relocation between tip-preparation areas, devices, and measurement sites. During operation, coarse alignment between tip and sample is performed in the upper chamber, and the corresponding capacitance value is recorded once the shuttle is docked in the DR. This value serves as a reference for subsequent position calibration. The sensing electronics apply a voltage pulse to an excitation pad, partially coupled to two measurement electrodes. In the Z walker (Fig. 3.4d), two fixed copper plates are mounted to the walker body and one to the moving slider. As the slider moves, the capacitive coupling between the two stationary plates changes, producing a differential signal proportional to position. The XY walker employs a similar four-quadrant sensor, see Fig. 4.5 in the Appendix, section 4.4, to track diagonal motion across the lateral plane. Because the sensing lines are sensitive to vibrational noise, the two measurement leads are twisted together before reaching the sensing electrodes, while the excitation lead is routed separately to minimize crosstalk and pickup.

The tip and sample stages (bottom of Fig. 3.4b) and their holders (Fig. 3.4e) are designed for reliable mechanical docking and electrical connectivity. Each stage uses BeCu spring contacts[101] that secure the holders within precision kinematic mounts while simultaneously providing multiple electrical connections (see Fig. 4.6 in the Appendix, section 4.5). These connections support sample gating, transport measurements, and switching between STM and AFM operation. The kinematic mounts employ three 1.5 mm sapphire hemispheres affixed with H72 epoxy, forming a triangular support pattern that ensures submicron repeatability upon reinstallation. To reduce mass, especially critical for the sample stage at the end of the piezo scan tube, the stages are machined from titanium and Macor. A ruthenium oxide thermometer[102] is mounted on the sample stage for temperature monitoring, and a small piezo shaker is attached to the probe stage for AFM excitation. The sample stage is mounted to the end of the piezoelectric scan tube, which is enclosed by a BeCu spring sleeve terminated with a grounded copper cap for electromagnetic shielding. The scan tube achieves a 13 μm × 13 μm lateral range with its first resonance at 1.8 kHz (additional information provided in the Appendix, section 4.3.3), providing both large area scans and high mechanical stiffness. All wiring for the sample and probe stages is routed through the shuttle base, and the sample-stage can be disconnected using an circular connector[103] for maintenance or disassembly. The probe stage rests on a pedestal with a rectangular cutout allowing for the fiber holder to enter into the microscope from the bottom of the docking station.

Powder filters are essential for reducing the electron temperature to values approaching the base temperature of the DR. In our implementation, we adopt a design inspired by Refs.[104,105], modified to improve compactness and high-frequency performance. As shown in Fig. 3.5a, our filter assembly differs by incorporating surface-mount NP0 chip capacitors rather than discoidal capacitors. To enhance broadband attenuation, we employ a combination of capacitors with different values. At high RF frequencies, real capacitors exhibit parasitic inductance that causes them to act inductively above a certain point. Each capacitor has a self-resonant frequency (SRF) where its capacitive reactance and inductive reactance cancel:

$$X_C = \frac{1}{2\pi f C}, \quad X_L = 2\pi f L$$

At resonance:

$$\frac{1}{2\pi f_{\mathrm{SRF}} C} = 2\pi f_{\mathrm{SRF}} L$$

Above f_{SRF}, the inductive term dominates, and the capacitor behaves like an inductor. Smaller capacitors have higher f_{SRF}, so RF designs often use several capacitor sizes in parallel to maintain effective attenuation across a wide frequency range.

The powder–epoxy composite core consists of a mixture of 10% epoxy, 80% Stycast 2850 FT with catalyst 23 LV and 20% Stycast 1266 by weight, and 90% metal powder by weight, potted inside a PTFE tube and cured in a vacuum oven at 60 °C. Each cylindrical core measures 1.2 inches in length and is wound with 34-gauge Kapton-coated copper wire. SMP connectors are attached by soldering chip capacitors between the inner pin and ground, and the end of the wound copper wire is soldered to the inner conductor (Fig. 3.5(a)). The completed assemblies are mounted in sets of four within gold coated copper cartridges (Fig. 3.5b) and potted with Stycast 2850FT, again cured at 60 °C under vacuum. This cartridge-style design allows multiple filters to be installed efficiently on the limited surface area of the mixing chamber (Fig. 3.5c).

The reflection spectra of these filters, measured up to 10 GHz, are shown in Fig. 3.5(d). Comparisons between powder-filled and pure PTFE-filled cores show similiar attenuation characteristics, suggesting that most high-frequency suppression arises from the combined capacitive and inductive elements rather than resistive dissipation in the metal powder via the skin effect. Additional discussion of these results is provided in the Appendix, section 4.6. Figure 3.5(e) presents a comparison between filters incorporating different capacitor combinations. The use of multiple capacitors in parallel effectively mitigates resonant transmission peaks at higher frequencies, as each capacitor compensates for the inductive response of others. This approach broadens the suppression bandwidth and yields smoother reflection characteristics over several frequency decades.

3.3.1 Atomic force microscope design

Cryogenic preamplifier and qPlus sensor integration

qPlus sensors have become a widely used platform for AFM due to their ease of implementation, high quality factors, reproducible atomic resolution, and flexibility in probe configuration. In our system, we integrate etched qPlus cantilevers provided by Giessibl[109] with magnetic nickel STM tips[110] and a cryogenic preamplifier, enabling magnetic force microscopy at the base temperature of the SPM.

The cryogenic preamplifier, shown in Fig. 3.6(a), employs a differential two-stage design illustrated in Fig. 3.6(b). A preamplifier located on one of the cryogenic stages is particularly beneficial for qPlus AFM operation, which is susceptible to capacitive pickup. By placing the preamplifier on the 4 K stage, we eliminate approximately one meter of coaxial cabling to the input, reducing parasitic capacitance and thermal noise. Operational amplifiers were selected to balance low-noise performance with low power consumption, since excessive dissipation would increase helium boil-off and compromise temperature stability. The circuit operates below a 3 V bias to further limit power dissipation. Resistors and capacitors were hand-selected from a matched batch to ensure closely

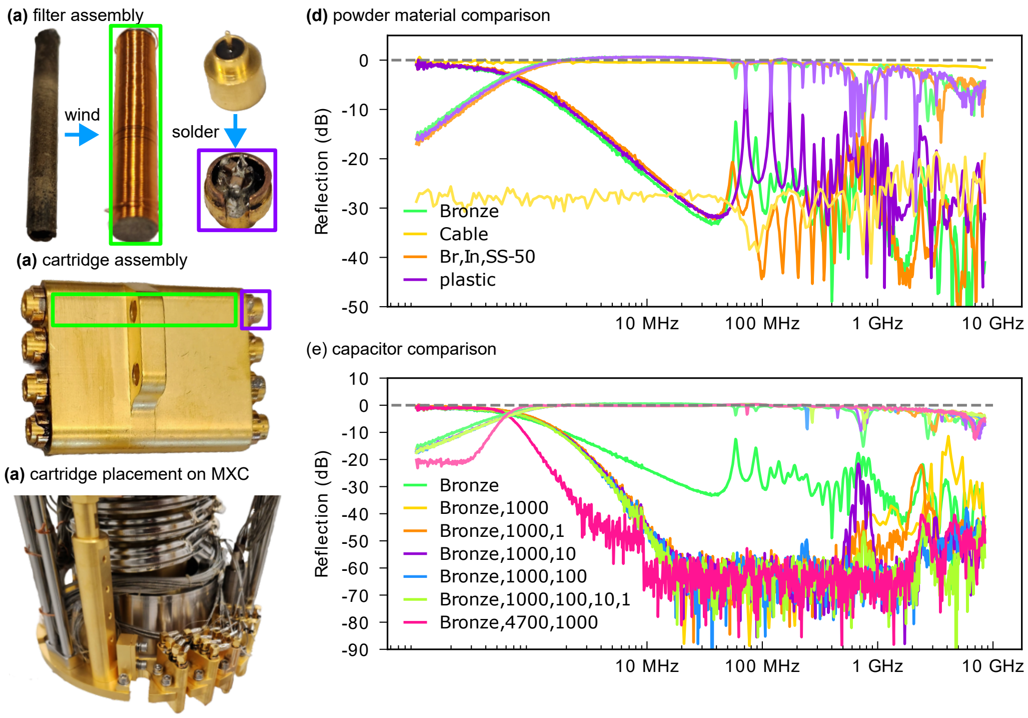

Figure 3.5: **(a)** Assembly process for the wound powder filters, showing the copper wire winding and soldered connector assembly. **(b)** Completed cartridge containing four filters mounted in parallel. **(c)** Installation of the cartridge on the mixing chamber (MXC) plate of the DR. **(d)** Reflection spectra comparing different powder materials and dielectric cores including bronze,[106] Br/In/SS-50 (equal amounts bronze, Inconel 625,[107] and Stainless Steel 316[108] by weight), cable, and PTFE. Minimal difference between powder-filled and PTFE cores indicates that high-frequency attenuation is dominated by capacitive and inductive components rather than skin-effect dissipation. **(e)** Comparison of reflection spectra for filters incorporating different capacitor combinations. Multiple capacitors in parallel reduce high-frequency resonances and extend broadband attenuation beyond 1 GHz. These measurements demonstrate the strong reflective behavior and effective noise suppression of the cartridge-style filters up to 10 GHz.

balanced values across differential input pairs.

The printed circuit board is fabricated from PTFE to provide vacuum compatibility and low thermal conductivity, minimizing heat conduction from the 4 K plate where the amplifier is mounted. Maintaining this temperature is critical, as the semiconductor elements in the amplifiers can experience carrier freeze-out at lower temperatures. Input and output connections are made using 40-gauge stainless-steel wiring for minimal thermal loading. The input uses SMP connectors, while the power and output lines use a circular micro-connector[103]. The preamplifier is enclosed in a gold-coated copper housing, which serves as both an electromagnetic shield and a thermal anchor.

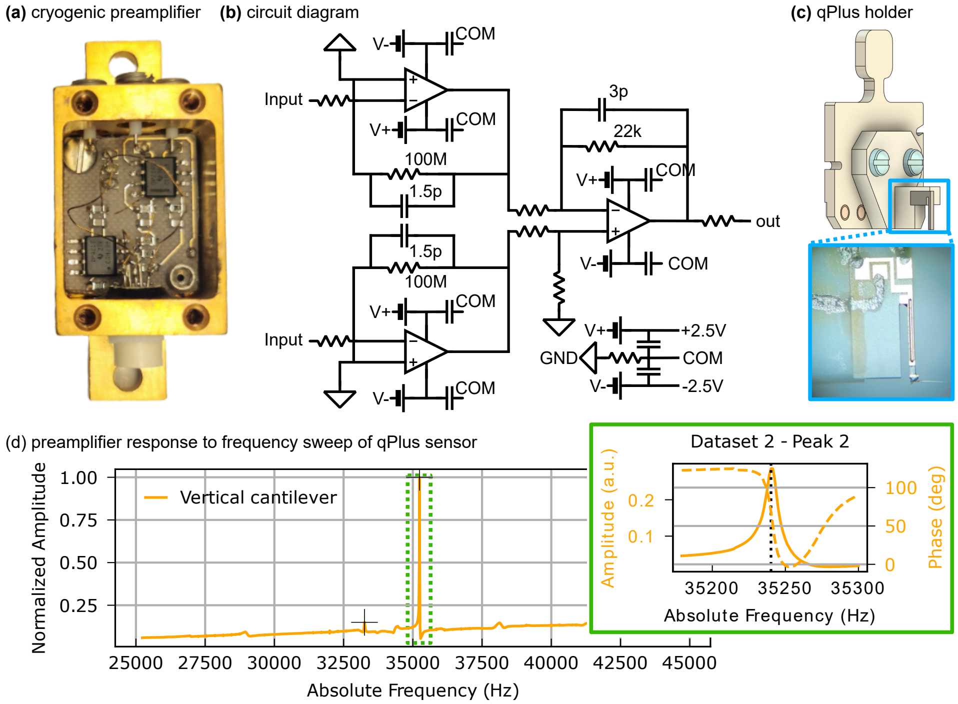

Figure 3.6: **(a)** Photograph of the assembled cryogenic preamplifier. **(b)** Schematic circuit diagram showing a low-noise differential amplifier that buffers two high-impedance inputs and combines them into a single amplified output using a summing stage. **(c)** Schematic of the qPlus sensor assembly, showing the Macor holder, glued cantilever,[109] and attached nickel STM tip. The inset illustrates the assembled sensor mounted to the probe stage. **(d)** Frequency response of the cryogenic preamplifier and qPlus sensor during a frequency sweep. The inset highlights the resonance peak and phase shift, demonstrating strong cantilever response and stable amplification.

The qPlus sensor is constructed by gluing an etched quartz cantilever onto a Macor holder, oriented either vertically or horizontally depending on the experimental geometry. A small amount of silver epoxy is applied to the free end of the cantilever to attach the final 0.4 mm of a nickel STM tip oriented perpendicular to the cantilever surface. Electrical contacts between the cantilever and Macor holder are also made with H20E silver epoxy. The assembled holder is mounted to a metallic baseplate and electrically connected via fine soldered wires. A completed assembly is shown in Fig. 3.6(c). In operation, twisted-pair wiring from the cryogenic preamplifier provides low-noise signal readout to the AFM input stage. A side-mounted piezoelectric shaker drives the cantilever at its mechanical resonance. Figure 3.6(d) shows a frequency sweep of the qPlus response, with the inset highlighting the resonance peak and phase transition, confirming the strong mechanical coupling and sensitivity of the assembled system.

SILICON CANTILEVER ATOMIC FORCE MICROSCOPY USING A FIBER INTERFEROMETER

The silicon cantilever remains the most common implementation of AFM in ambient and moderate vacuum environments, though its use has become less prevalent in cryogenic systems as qPlus sensors have gained popularity for their simpler integration and reproducible atomic-scale resolution. Nevertheless, silicon cantilevers offer distinct advantages, including their wide commercial availability and the extensive range of customizable parameters such as length, stiffness, coating, and resonance frequency. Their relatively low stiffness is especially advantageous in quantum materials research, as it enables enhanced force and dissipation sensitivity at the expense of spatial resolution.

The main challenge in employing silicon cantilevers in cryogenic environments lies in the complexity of optical detection and alignment. While optical beam deflection[7] is widely used in conventional AFM systems, it requires in-situ placement of mirrors and photodetectors, which complicates cryogenic operation. Instead, we implement a fiber-based interferometric detection system following the designs of Refs.[9]. The overall optical layout is shown in Fig. 3.7(a). A 633 nm laser diode[111] provides a narrow-linewidth light source driven by a stabilized laser controller[112] and attenuated to control the incident power[113]. A fiber circulator[114] directs light toward the cantilever and routes the reflected signal back to a photodetector[115]. The optical fiber,[116] clamped to each thermal stage of the DR, terminates near the cantilever. Partial reflection occurs at the fiber–vacuum interface and again at the cantilever surface, producing an interference signal that depends on the relative phase between the two reflected paths. As the cantilever oscillates, the phase difference varies, modulating the detected optical power. This configuration minimizes the number of in-situ components to a single fiber, simplifying cryogenic integration.

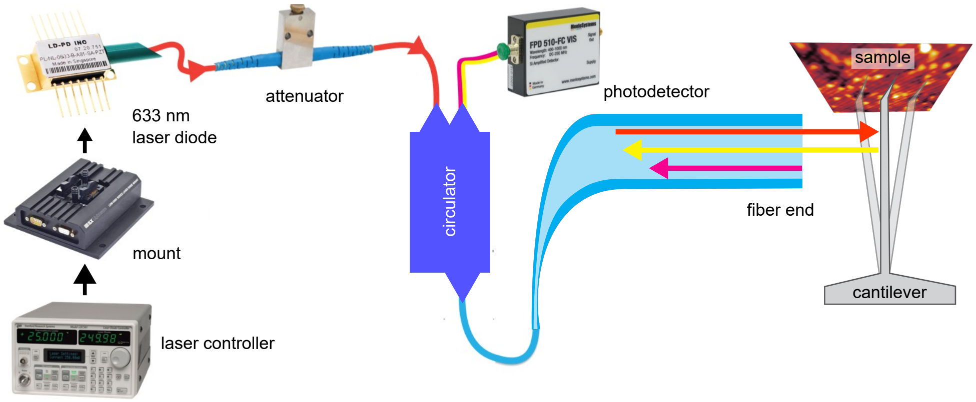

Figure 3.7: Schematic of the fiber-interferometric detection setup. A 633 nm laser diode held in a temperature stabilized mount[117], driven by a stabilized laser controller, provides the optical excitation. The beam passes through an attenuator and circulator, which directs light to the cantilever through an optical fiber and routes the reflected interference signal to a photodetector. The resulting interference between reflections at the fiber end and the cantilever surface enables displacement detection with sub-picometer resolution while minimizing in-situ optical components.

Given the typical dimensions of silicon cantilevers (∼100 µm in length and sub-10 µm in width), precise optical alignment is critical. We achieve this using a custom three-axis piezo motorized fiber positioner (Fig. 3.8a). The system consists of a Pan-style walker[100] providing 10 mm of coarse motion and two single-axis piezo walkers stacked above it (Fig. 3.8c), each offering 1.5 mm of range. The decoupled design minimizes drift and cross-talk between axes during alignment. Additionally, a piezo stack is mounted at the base of the fiber arm (Fig. 3.8b), enabling fine positional adjustments to compensate for low-frequency thermal drift and maintain operation near the quadrature point of the interferometric signal. The fiber end is aligned to within 1 µm of the cantilever (Fig. 3.8(d)) for optimal interference contrast, allowing stable operation.

The interferometric signal measured while retracting the fiber from the cantilever surface is shown in Fig. 3.9. At large separations the reflected amplitude decays exponentially due to reduced optical overlap, while within approximately 1 µm the system operates in the highest-sensitivity

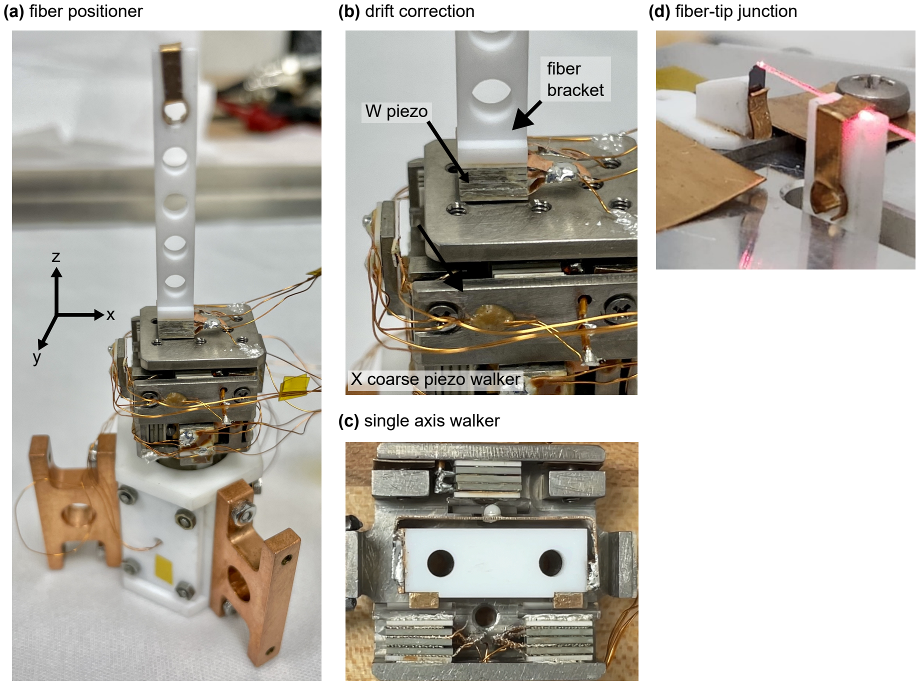

(a) fiber positioner

(b) drift correction

(c) single axis walker

(d) fiber-tip junction

Figure 3.8: **(a)** Three-axis fiber positioner used for optical alignment of the interferometer. **(b)** Zoomed view showing the fiber bracket and piezo stack used for drift correction and fine distance control. **(c)** Single-axis piezo walker module providing precise motion along X and Y individual axes. **(d)** Fiber–tip junction during alignment, showing laser light reflection from the cantilever surface. The combined setup enables sub-micron positioning precision and stable long-term alignment within the DR.

regime. This working distance, typically less than ten wavelengths ($< 10\lambda$), provides optimal interferometric contrast and minimizes.

The amplitude resolution of the interferometer was characterized by driving the cantilever with a modulated piezo signal while monitoring the detected oscillation amplitude (Fig. 3.10(a)). The measurement noise floor, corresponding to the system's amplitude sensitivity, was found to be below 190 fm for a 130 μW optical power beam. This sub-picometer resolution demonstrates that the fiber interferometer achieves the sensitivity required for dissipation and force measurements in the pendulum AFM configuration. In Fig. 3.10(b), ultimate resolution for several different laser powers and for an additional add-on amplification stage are demonstrated.

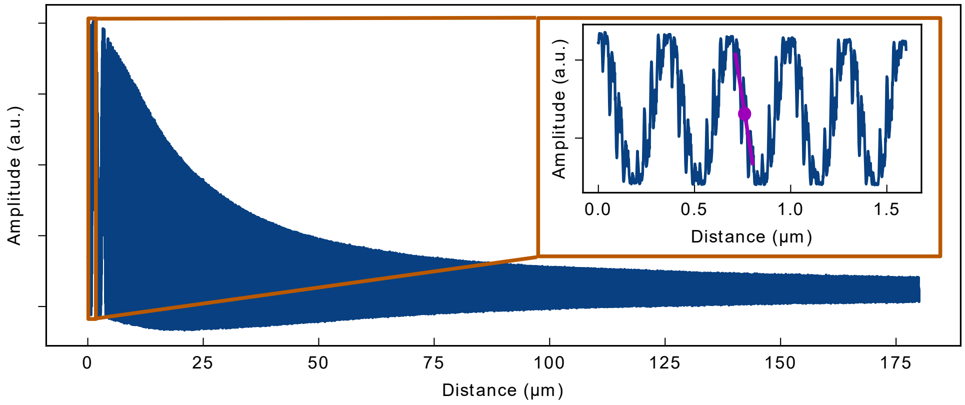

Figure 3.9: Measured interferometric signal amplitude as a function of fiber–cantilever distance. The amplitude decreases exponentially with separation, with the inset showing the highest-sensitivity regime at sub-micron distances ($< 10\lambda$) between the fiber and cantilever. The purple marker indicates the quadrature point, where phase sensitivity to displacement is maximized.

3.4 BASE TEMPERATURE STM MEASUREMENTS

3.4.1 SCANNING TUNNELING MICROSCOPE NOISE AND ELECTRON TEMPERATURE

The results of the STM and STS characterization are presented in Fig. 3.11. Despite the large number of electrical connections entering the microscope, the implemented filtering and isolation strategies effectively suppressed electronic noise, allowing atomic resolution imaging on $NbSe_2$ at 4 K (Fig. 3.11a). The corresponding fast Fourier transform (FFT) of the topographic image (Fig. 3.11b) clearly resolves both the primary Bragg peaks and the charge density wave (CDW) satellite peaks, confirming the system's spatial resolution and stability. The frequency spectrum for both in-tunneling and out-of-tunneling is presented in Fig. 4.8 in the Appendix, section 4.7. At the base temperature of the DR, differential conductance spectra of the $NbSe_2$ superconducting gap were acquired (Fig. 3.11c). The data were fit using the Dynes function for the superconducting density of states,[118] yielding an effective electron temperature between 370 mK and 885 mK depending on the fitting parameters. Details of the Dynes function as well as the Maki function and fitting are given in the

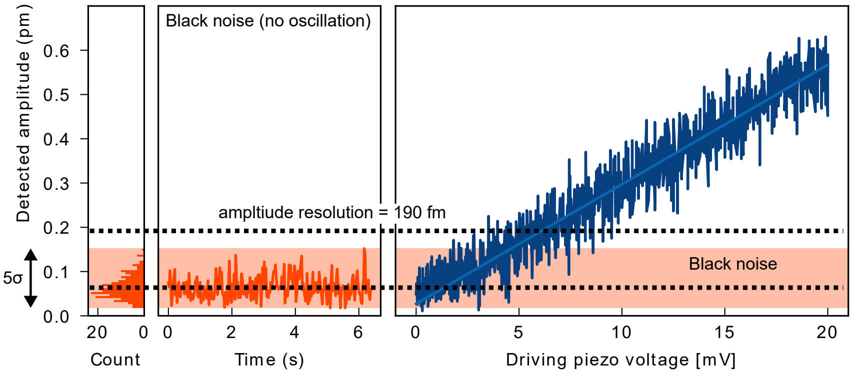
(a) cantilever oscillation noise floor

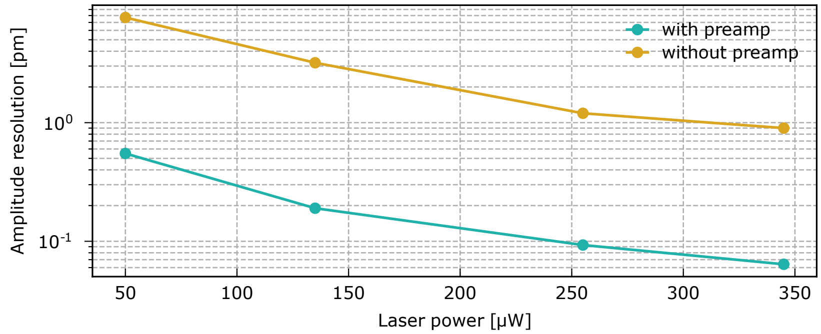
(b) cantilever ultimate resolution vs. laser power

Figure 3.10: (a) Characterization of the interferometric amplitude sensitivity. Left: histogram and time trace of the measured background noise with no cantilever excitation. Right: detected amplitude as a function of piezo drive voltage, showing a linear response above the noise floor. The shaded region indicates the black noise level, corresponding to an amplitude resolution of 190 fm for a 100 μW optical beam. **(b)** Amplitude sensitivity vs laser power after the attenuator. The blue orange curve shows the values taken directly from the photodetector[115] while the orange curve shows values for a x1000 amplified photodetector output.

Appendix, section 4.8. These measurements demonstrate both the spectroscopic precision and noise performance of the system at millikelvin temperatures. For a true determination of the electron temperature, the tip-sample junction stability will need to be improved.

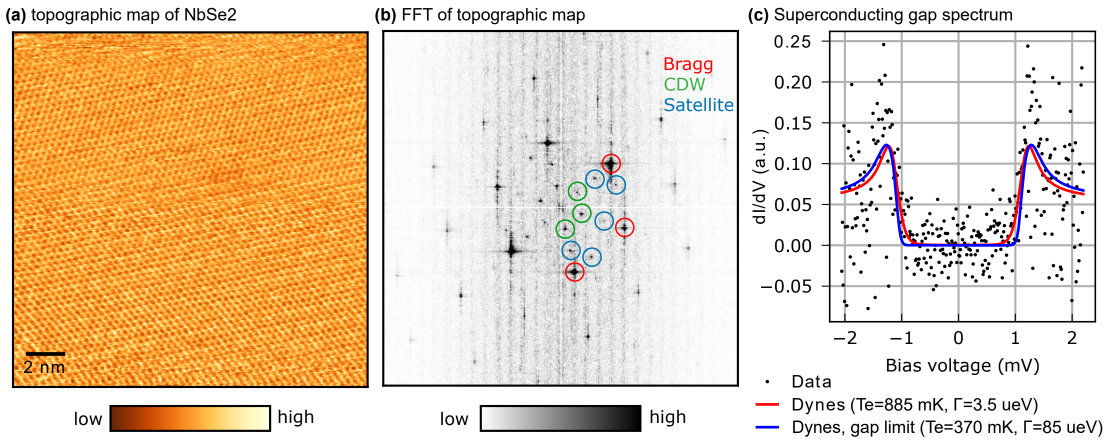

Figure 3.11: (a) Atomically resolved STM topographic image of $NbSe_2$ acquired at 6 K ($V_s = 25$ meV, $I_s = 130$ pA), showing the hexagonal lattice with a periodic modulation from the charge density wave. **(b)** Fast Fourier transform (FFT) of the topographic image, highlighting the Bragg peaks (red circles), CDW peaks (green circles), and higher-order satellite peaks (blue circles). **(c)** Differential conductance spectrum of the $NbSe_2$ superconducting gap measured at 63 mK ($V_s = -10$ meV, $I_s = 100$ pA, $V_{mod} = 7\ \mu$eV). The data (black dots) are fit with the Dynes model,[118] yielding an effective electron temperature between 370 mK and 885 mK.

3.5 Conclusion

The development of this millikelvin SPM represents a versatile and stable platform for studying quantum materials and device structures at the lowest accessible temperatures. Through the integration of compact two-stage vibration isolation, a modular UHV-compatible cryostat, and a high-density wiring architecture with extensive RF filtering, the system achieves both mechanical rigidity and low electronic noise. The modular shuttle design combines STM and AFM functionality within a single cryogenic head, incorporating three-axis nanopositioning, capacitive sensing, and interchangeable probe holders optimized for STM, qPlus AFM, and silicon-based pendulum AFM operation.

Demonstrations of atomic resolution imaging on $NbSe_2$, superconducting gap spectroscopy, and millikelvin electron temperatures confirm the successful performance of the system. Together, these results establish a foundation for future experiments exploring correlated, topological, and dissipative phenomena in quantum materials. The flexibility and modularity of the design also provide a clear path toward implementing additional capabilities such as multi-probe operation and advanced dissipation or transport measurement modes.

4

Appendix

4.1 Band structure and DOS comparison

The formation of a van Hove singularity (VHS) in the density of states (DOS) due to Rashba spin-splitting of a two-dimensional (2D) surface band is well-established[68,64], and schematized here in Fig. 4.1.

The formation of the VHS is hard to visualize when projected onto one dimension (1D), as in

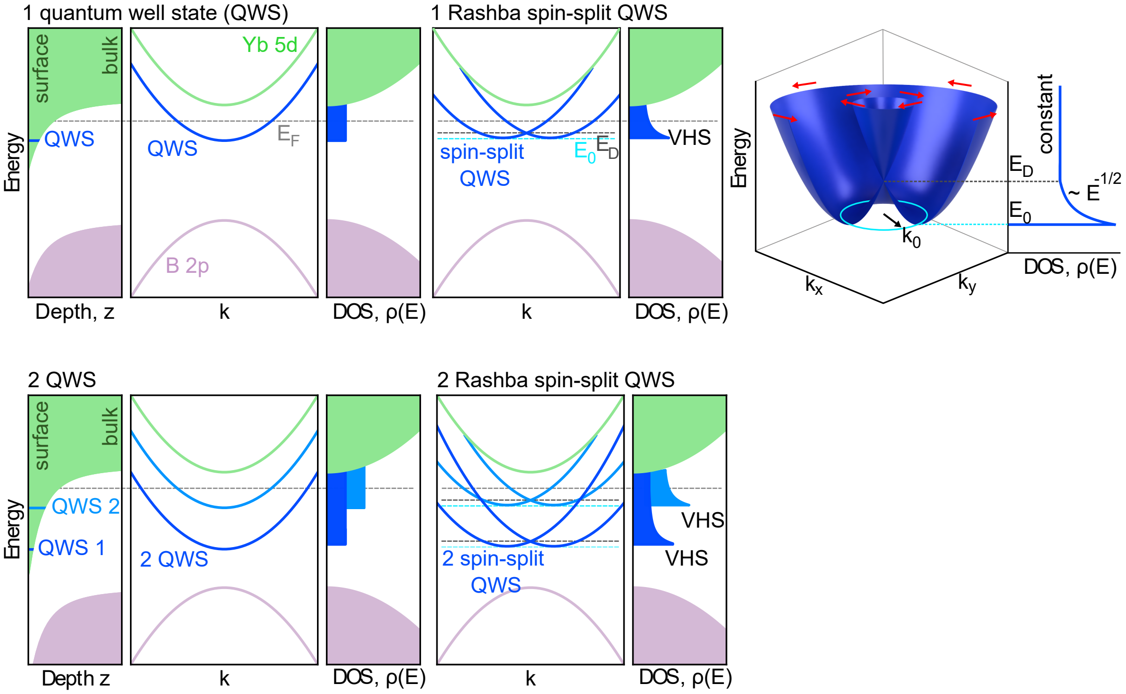

Figure 4.1: Schematics comparing the surface band bending, band structure, and density of states (DOS) for several scenarios of quantum well states (QWS) and Rashba spin-splitting. **(a)** Single QWS. Left: n-type band-banding is expected on surface terminations such as Yb or partial B_n, where bulk free electrons accumulate at small depth z to compensate the net positive ionic charge. When the bulk conduction band bends below the Fermi level E_F, in a confined "quantum well" region close to the surface, a new 2D state appears, shown here in blue at its Γ-point energy. Middle: 1D cut along k_x (same as k_y), showing $E(k)$ for the 3D bulk bands (green, purple) and 2D surface QWS band (blue). All bands are spin-degenerate. Right: Density of states (DOS), $\rho(E)$, is the k-integral of the band structure. The 2D integral of a single parabolic QWS gives a step function (blue) with constant value above the onset energy. The 3D integral of a parabolic bulk band is proportional to $E^{3/2}$ (green, purple). **(b)** Rashba spin-splitting of the single QWS. Left: at each k, the surface state (blue) splits vertically by $\Delta E = \alpha\hat{z} \cdot \boldsymbol{k} \times \sigma$ where α is the Rashba parameter and σ is the spin vector[60]. In a 1D slice, the k-dependent *vertical* energy splitting gives the appearance of two parabolas shifted *laterally*, with Dirac point at E_D (gray) and energy minimum E_0 (cyan). Right: 2D k-integral of the spin-split QWS gives a van Hove singularity (VHS) in the DOS at E_0. **(c)** 2D view of the Rashba spin-split QWS shows how a ring of degenerate states (cyan) emerges at the energy minimum E_0, giving rise to a VHS in the DOS. **(d)** Same as (a) but for a deeper quantum well (more band-bending, e.g. from more positively-charged surface ions), which allows two QWS. **(e)** Rashba spin-splitting of two QWS gives two VHS in the DOS.

Fig. 4.1(b) (loosely adapted from Fig. 2 in Ast *et. al.*[68]) However, in Fig. 4.1(c) (loosely adapted from Fig. 1 in Berg *et. al.*,[59]) we show the full 2D diagram of Rashba spin-splitting, which clarifies how the total number of states at the parabolic band extremum (here labeled E_0) increases from a point to a ring when the band splits, thus giving rise to the VHS. The VHS arises generally at the outer band edge, and does not depend on hybridization between bands at their crossing point.

4.2 CHAIN SURFACE TERMINATION

We identify the chain surface as boron-terminated, based on its half-unit-cell lateral offset and its band-bending with respect to the 1×1 surface, but we are not able to determine the exact boron configuration. In Fig. 3(d) of the main text, we showed the B_4 termination as one example, but in Fig. 4.2 we show other possible partial boron chain terminations from two perspectives, including B_2, B_3, B_4, tilted B_5, and tilted B_6. The tilt angle of the partial boron octahedra may also vary for each of the possible terminations in Fig. 4.2.

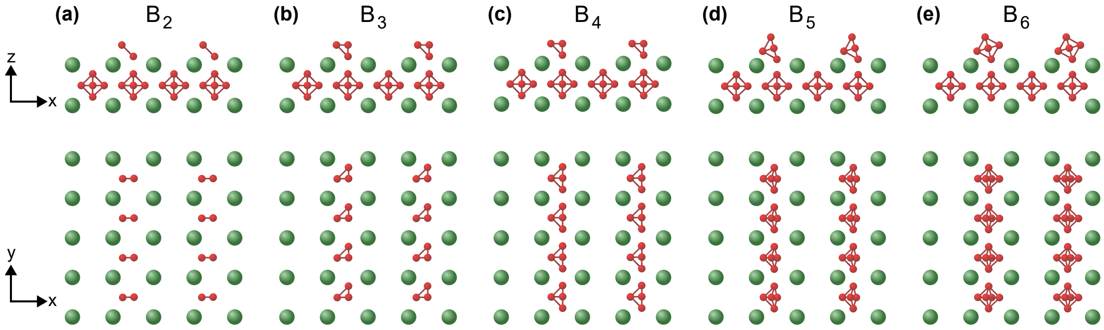

Figure 4.2: Side and top views of five possible chain surface terminations composed of partial boron octahedra: **(a)** B_2, **(b)** B_3, **(c)** B_4, **(d)** tilted B_5, and **(e)** tilted B_6 octahedra.

4.3 Resonance modes of room and microscope head

4.3.1 Table resonance mode comparisons

In many high-resolution, low-temperature STM systems, stacked pneumatic air-leg isolation stages are commonly used to suppress environmental vibrations.[119,120,104] However, in our setup, the room height imposed strict constraints on the total isolation stack height. When evaluating a stacked air-leg configuration, we found that it required suspending the secondary isolation platform (the lead-loaded table) from the upper air legs. Finite-element simulations of this geometry, shown in Fig. 4.3(a), revealed low natural resonance modes near 91 Hz. In addition to the low mechanical stiffness, this configuration placed the center of mass well below the optimal operating point of the air legs, which are designed for maximum stability when the load is centered near the top of the isolators. This mismatch leads to undesirable rocking and coupling modes.

To overcome these limitations, we replaced the secondary pneumatic stage with compact elastomer isolators positioned directly beneath the lead-loaded table. This modification allows the table to rest securely on top of the isolators rather than being suspended from them, improving load distribution and shifting the system's center of mass closer to the isolator's effective damping region. The resulting mechanical model, shown in Fig. 4.3(b), exhibits a higher lowest resonance mode at 115 Hz, providing both improved rigidity and reduced mechanical cross-coupling between the support structure and the microscope.

4.3.2 Resonance modes of stacked walker design

To enable three-axis sample positioning relative to the tip, we employed a stacked walker configuration in which an XY plate walker is mounted atop a Pan-style Z walker. While such stacked designs offer compactness and flexibility, they are also prone to lower mechanical resonance frequencies,

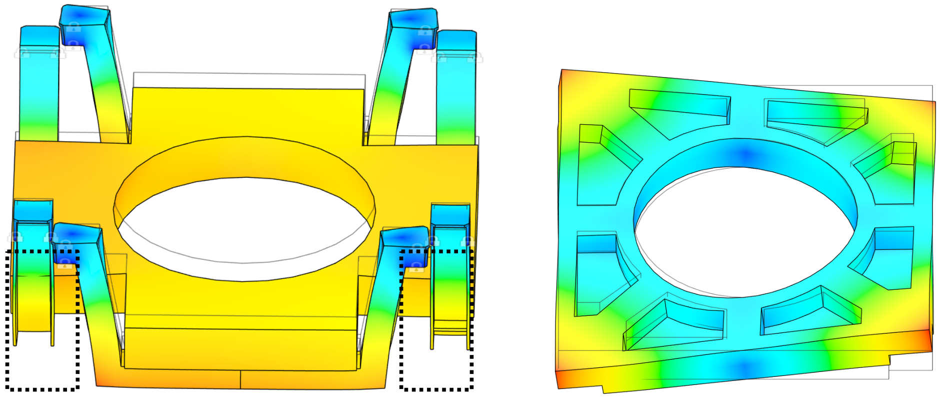

(a) table lowest resonance mode for air leg supports

(a) table lowest resonance modes for elastomer supports

lowest resonance mode = 91 HZ

lowest resonance mode = 115 HZ

Figure 4.3: Finite-element simulation of the lowest mechanical resonance modes for two table support configurations. **(a)** The stacked pneumatic air-leg design, where the secondary table is suspended from the isolators, exhibits a fundamental resonance at 91 Hz and an unfavorable center-of-mass position below the top of the isolatr. **(b)** The elastomer-based support design raises the lowest resonance to 115 Hz and provides a more favorable load geometry, with the center of mass nearer the elastomer's top surface. The elastomer configuration offers improved damping efficiency and overall mechanical stability within the height limitations of the laboratory.

a significant concern for scanning probe heads that require high stiffness to minimize vibrational coupling. To ensure adequate rigidity, multiple geometries were simulated to identify a configuration with resonance frequencies well above the operational cutoff of approximately 3 kHz. Finite-element simulations of different designs are presented in Fig. 4.4, culminating in the optimized geometry shown in Fig. 4.4(c), which achieves a lowest resonance mode of $\sim$5.5 kHz. This configuration provides a balance between travel range and mechanical stability suitable for cryogenic operation.

4.3.3 RESONANCE MODES OF PIEZO-ELECTRIC SCANNER

A common source of of low frequency modes in SPM heads is the piezo-electric scanner. The scanner naturally possess a tradeoff between increasing scan range and decreasing natural resonance modes. The deflection in X, Y, and Z are given by the following equations:

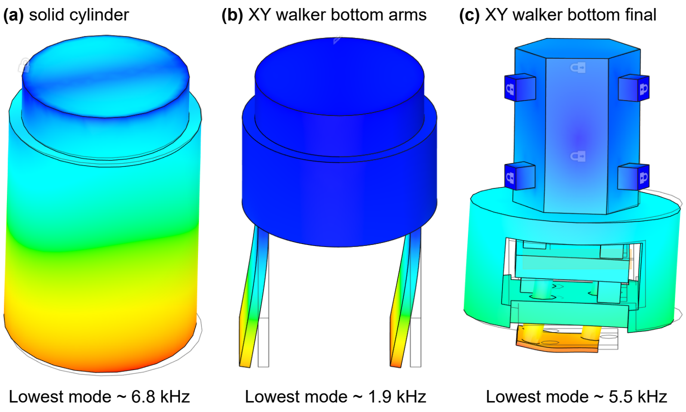

Figure 4.4: Finite-element simulation of resonance modes for successive iterations of the stacked walker design. **(a)** A solid cylinder geometry exhibits a high stiffness with a lowest resonance mode at ∼6.8 kHz but offers no lateral motion. **(b)** Introducing flexure arms to enable XY motion significantly reduces the lowest mode to ∼1.9 kHz, limiting rigidity. **(c)** The final optimized design for the XY walker incorporates reinforced base and arm structures, restoring stiffness and achieving a lowest resonance frequency of ∼5.5 kHz. This configuration ensures sufficient mechanical stability for high-resolution scanning while maintaining the required nanopositioning range.

$$\Delta x = V_x \frac{2\sqrt{2}d_{31}L^2}{\pi D h}, \Delta y = V_y \frac{2\sqrt{2}d_{31}L^2}{\pi D h}, \Delta Z = V \times \frac{d_{31}L}{h}. \tag{4.1}$$

Where d_{31} is the piezoelectric strain constant, L is the length of the tube, D is the outside diameter, h is the tube thickness, and V_x and V_y are the electrode voltages. The deflection in X, Y, and Z both increase with increasing L but the fundamental mode of a pendulum system also scales as $L^{-1/2}$ and also decreases with the additional weight of the sample stage. As such, we chose to limit the theoretical lowest frequency mode of the scan tube to above 2 kHz with the added mass of the sample stage on the end while keeping the room temperature scan range in XY to $\sim 13\mu m$.

4.4 CAPACITANCE SENSOR LAYOUTS

The capacitance sensors use a differential style measurement employing. In Fig. 4.5(a,b), the layouts for the Z capacitance sensor and XY capacitance sensor are shown. The XY design minimizes the number of excitation plates needed by using the same excitation plate for both the X and Y measurements.

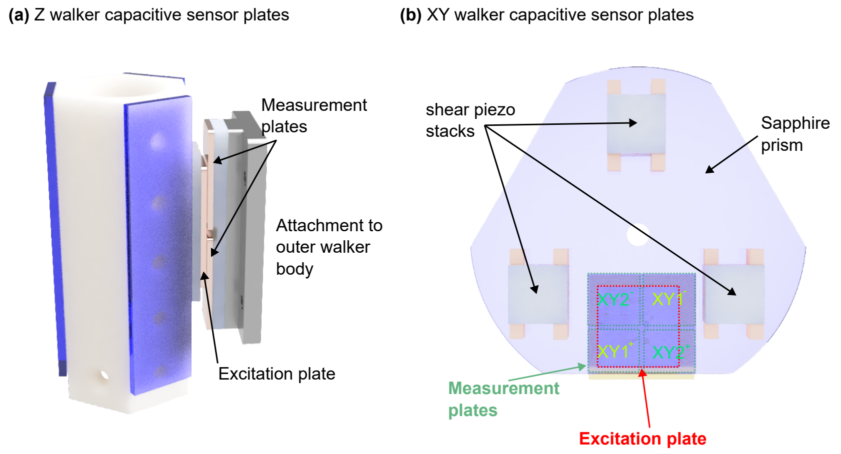
(a) Z walker capacitive sensor plates
(b) XY walker capacitive sensor plates

Figure 4.5: **(a)** The Z walker capacitive plate layout. The central prism has a copper pad glued to one of the exposed Macor sides that acts as the excitation plate. On the outer body of the Z walker, two copper plates are separated by a small gap. As the Z walker actuates, the difference in the area between the two plates changes leading to a change in the differential capacitance measured. **(b)** The XY walker capacitive plate layout. A copper plate is glued to a stand-off on the sapphire plate and acts as the excitation plate. Four thin copper foil electrodes are glued to the base of the XY walker and positioned with a small gap between each electrode and the excitation plate. The differential measurement is taken between the diagonals of the electrode plates and together the two values allow for an measurement of the XY position of the sapphire plate.

4.5 MULTIPLE STAGE CONTACTS AND KINEMATIC STAGE MOUNTS

The sample and probe stages provide several contacts for different probe measurements (including qPlus AFM and RF applications) and sample applications (gating, transport, etc.) as shown in Fig. 4.6. Additionally, it is desirable to have the tip and sample holders interface to the same position within the stages between transfers. This allows for more accurate tip positioning over the sample, ensuring devices are within the XY walker range, repeatability of the AFM cantilever position with respect to the fiber, making it easier to align, and also allows for small flakes or devices to be more reliably found again between tip or sample transfers. The layout for the kinematic mount is shown in Fig, 4.6(b).

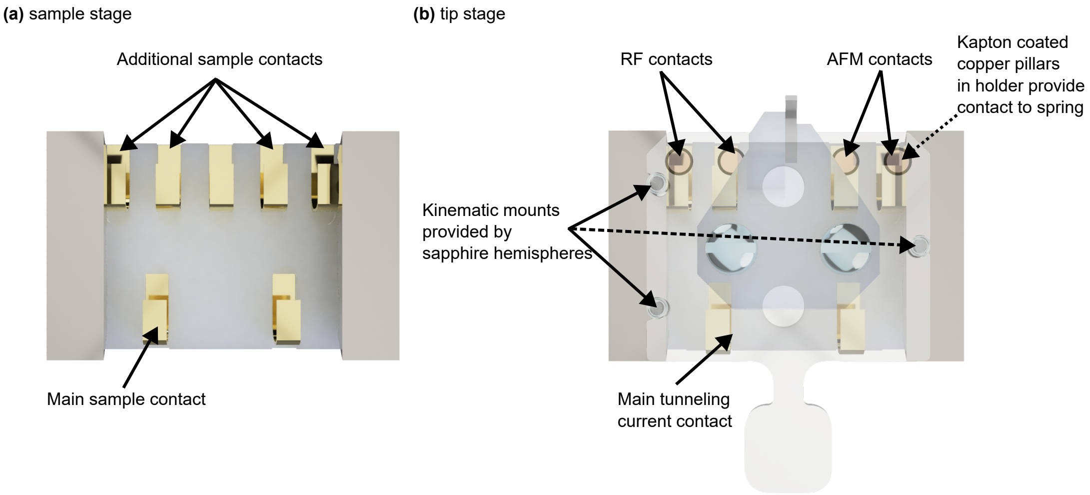

Figure 4.6: (a) The sample stage. Five contacts are available on the sample stage through BeCU springs that also act to tension the sample holder in the stage. Four contacts are provided on the upper springs in the panel and one contact, acting as the main contact, is provided on the lower spring. By applying a insulating coating, such as kapton tape, to the sample holder, different contacts can be prevented from making contact with the holder. **(b)** The probe stage. The main current contact is provided by one of the lower springs making contact with the probe holder baseplate. The four upper springs provide RF contacts as well as the qPlus AFM contacts for measurements of the cantilever oscillations. These contacts are routed through kapton-coated copper pillars that make contact with the BeCu springs. The kinematic mounting for the holder and stage is also illustrated where three sapphire hemispheres are positioned in a triangle formation within the probe stage and interface into channels cut into the probe holder. The BeCu springs push the probe holder up into the hemispheres ensuring repeatable interfacing.

4.6 SIMPLIFIED POWDER FILTER GEOMETRY MEASUREMENTS

To isolate the effect of fine metal powders on filter attenuation, we constructed a simplified test geometry consisting of a straight wire inside a cylindrical cavity that could be filled with various metal powders for broadband characterization. The proposed dissipative mechanism of these filters arises from attenuation through the skin effect, which should depend on both the electrical resistivity and the grain diameter of the metal powder.[121] The skin depth,

$$\delta = \sqrt{\frac{2\rho}{\mu\omega}}, \tag{4.2}$$

determines the characteristic penetration of electromagnetic fields into the conductor, where ρ is the resistivity, μ is the magnetic permeability, and $\omega = 2\pi f$ is the angular frequency. When the particle diameter d becomes comparable to or smaller than δ, the effective coupling to the electromagnetic field changes significantly, leading to frequency-dependent dissipation. The attenuation constant approximately follows

$$\alpha \propto \frac{1}{\delta}, \tag{4.3}$$

and the characteristic cutoff frequency can be estimated by setting $\delta \sim d/2$, yielding

$$f_c \propto \frac{1}{\mu}\frac{\rho}{d^2}. \tag{4.4}$$

Hence, decreasing the grain size or increasing the resistivity shifts the onset of dissipation to higher frequencies.

To test this dependence, several metallic powders were examined, and the samples were further sieved into particle-size fractions below 50 μm to evaluate the role of grain size on attenuation behavior. Figure 4.7(a) compares the transmission and reflection spectra for an unfilled cavity versus a bronze powder-filled cavity. The powder-filled configuration exhibits a cutoff frequency near 1 GHz and approaches the measurement noise floor by 10 GHz. The reflected signal remains stable around -10 dB, indicating approximately 10% reflection at the cavity interface. Figure 4.7(b) presents data for Inconel 625, stainless steel 316, and bronze powders with various size ranges. Across all materials and size fractions, the attenuation behavior is nearly identical, suggesting that the dominant high-frequency suppression mechanism is not governed by the skin effect but rather by dielectric loss and scattering within the powder matrix.

(a) straight filter comparison to empty enclosure

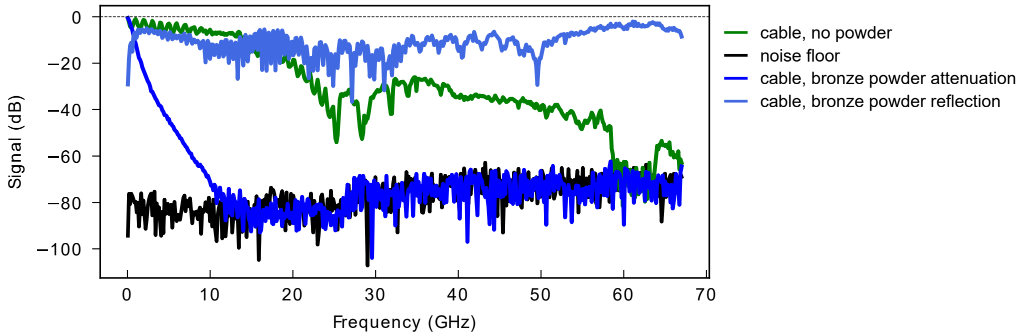

(b) powder material and diameter comparison

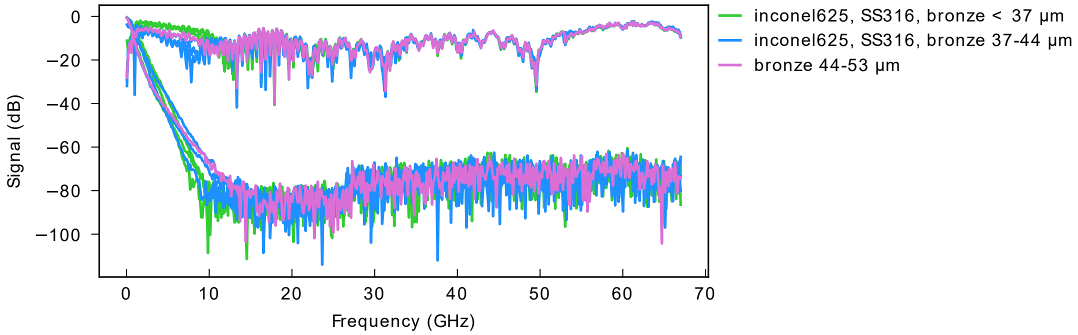

Figure 4.7: **(a)** Measured transmission and reflection spectra for a straight filter cavity either empty (green) or filled with bronze powder (blue). The powder-filled cavity exhibits strong attenuation above 1 GHz and approaches the noise floor by 10 GHz, with consistent reflection near -10 dB. **(b)** Comparison of powder material and grain size, showing similar attenuation for Inconel 625, stainless steel 316, and bronze powders across particle size ranges below 53 μm. The comparable response across all samples suggests that attenuation is primarily due to dielectric losses within the packed powder rather than skin-effect dissipation.

4.7 STM tunneling noise spectrum at cryogenic temperatures

A common benchmark of the noise performance in STM is visualized through the frequency spectrum both in-tunneling and out-of-tunnneling. This data is plotted in Fig. 4.8. Both data for 4 K operation and base temperature operation is provided for the in-tunneling spectrum. In both curves, there is a higher level of background noise at lower frequencies combined with a $\sim$ 10 Hz peak in the 4 K plot. The lower frequency noise is most likely from vibrational coupling which may result from reduced isolation performance possibly from the coupling of the gas handling system pumping lines. There are also a number of high frequency peaks present in the base temperature spectrum data. While the prominence of such peaks is not seen in the 4 K data, it is possible that additional noise from running the dilution circuit couples to existing modes within the microscope head assembly making the modes more obvious. Overall, the base temperature spectrum has a higher background noise level. This may be due to additional noise from running the gas handling system pumps, the dilution circuit, or possibly poorer tip stability.

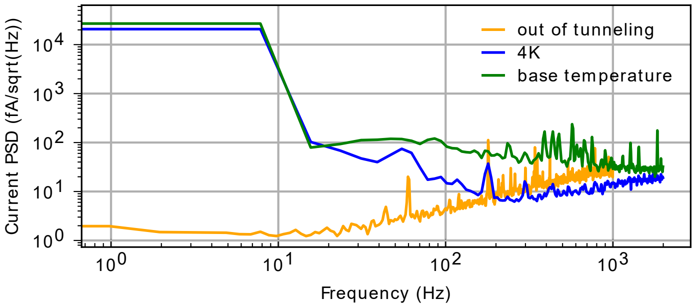

Figure 4.8: Noise spectrum of the STM both in and out of tunneling (orange). The in-tunnneling data is presented for both the 4 K temperature operation (blue), where the liquid helium bath is solely responsible for cooling the microscope head, and for base temperature (green), where the DR is active.

4.8 Dynes and Maki density of states functions

To extract the superconducting gap Δ and effective electron temperature T_{eff}, tunneling spectra were fitted using broadened BCS-type density-of-states (DOS) models that incorporate quasiparticle damping and pair-breaking effects. The analysis follows the formalism described in Machida *et al.*[122]

The measured differential conductance $g(V) = dI/dV$ is modeled as a convolution of the superconducting DOS $\rho(E)$, the derivative of the Fermi–Dirac distribution $f(E)$, and the instrumental lock-in broadening function $b(V)$:

$$g(V) = -\int_{-\infty}^{\infty} \left[\int_{-\infty}^{\infty} \rho(E) f'(\varepsilon + E)\, dE \right] b(eV - \varepsilon)\, d\varepsilon, \tag{4.5}$$

where e is the electron charge, and V is the applied bias voltage.

The derivative of the Fermi function is

$$f'(\varepsilon) = -\beta \frac{e^{\beta\varepsilon}}{(1 + e^{\beta\varepsilon})^2}, \quad \beta = (k_B T_{\text{eff}})^{-1}, \tag{4.6}$$

and the lock-in broadening due to a sinusoidal modulation amplitude V_{mod} is given by

$$b(V) = \begin{cases} \dfrac{\sqrt{2}}{\pi V_{\text{mod}}} \sqrt{1 - \left(\dfrac{V}{\sqrt{2} V_{\text{mod}}} \right)^2}, & |V| \leq \sqrt{2} V_{\text{mod}}, \\ 0, & |V| > \sqrt{2} V_{\text{mod}}. \end{cases} \tag{4.7}$$

4.8.1 Dynes Broadening Model

Finite quasiparticle lifetimes are incorporated phenomenologically using the Dynes function[118]:

$$\rho_D(E) = \text{Re} \left[\frac{E - i\Gamma}{\sqrt{(E - i\Gamma)^2 - \Delta^2}} \right], \tag{4.8}$$

where Γ is the quasiparticle damping parameter.

The parameter Γ accounts for inelastic scattering, coupling to phonons, or electronic noise. In STM experiments, Γ can also capture instrumental effects such as residual radio-frequency (RF) noise or tip–sample instability. Increasing Γ suppresses the coherence peaks and increases the subgap conductance (Fig. 4.9(a)).

4.8.2 MAKI PAIR-BREAKING MODEL

Pair-breaking effects from Pauli paramagnetism are modeled by the Maki function[123,124]:

$$\rho_M(E) = \mathrm{Re}\left(\frac{u}{\sqrt{u^2-1}}\right), \tag{4.9}$$

where u is a complex function of reduced energy $\varepsilon = E/\Delta$ and the dimensionless pair-breaking parameter ζ:

$$u = \frac{1}{2}\left(|\varepsilon| + \sqrt{1-\zeta^2+d}\right) + \frac{1}{2}\frac{1+\varepsilon^2-\zeta^2-d-2|\varepsilon|(1+\zeta^2)}{\sqrt{1-\zeta^2+d}}, \tag{4.10}$$

$$b = \varepsilon^2+\zeta^2-1, \tag{4.11}$$

$$c = 108\varepsilon^2\zeta^2+2b^3+\sqrt{(108\varepsilon^2\zeta^2+2b^3)^2-4b^6}, \tag{4.12}$$

$$d = \frac{b^3}{3}+\frac{2^{1/3}b^2}{3c^{1/3}}+\frac{c^{1/3}}{3\times 2^{1/3}}. \tag{4.13}$$

The parameter ζ quantifies the strength of pair breaking caused by magnetic impurities or currents. Unlike Γ, which broadens the DOS via lifetime effects, ζ maintains sharp edge in the corners of the gap (Fig. 4.9(b)).

4.8.3 COMPARISON AND INTERPRETATION

Both approaches capture deviations from the ideal BCS density of states but reflect different microscopic origins. In Machida *et al.*,[122] both models yielded consistent $T_{\text{eff}} \approx 90$ mK, while the Maki model provided slightly improved agreement.

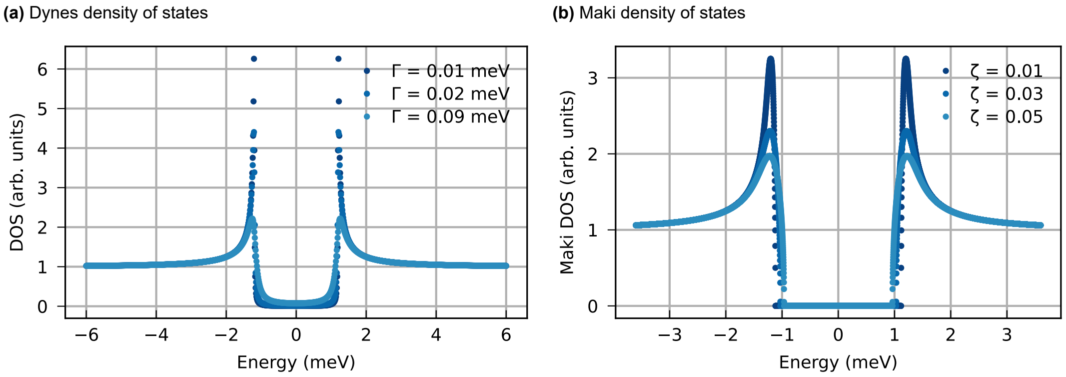

Figure 4.9: Temperature-dependent tunneling spectra of a $\Delta = 1.2$ meV superconducting gap measured with a metallic tip. Each curve shows the differential conductance dI/dV at zero temperature. For the Dynes **(b)** and Maki **(a)** simulated gaps, their phenomenological damping parameters are increased resulting in an apparent broadening of the coherence peaks and a reduction in the gap size.

4.8.4 NBSE$_2$ SPECIFIC GAP NUANCES AND MODEL CHOICE

NbSe$_2$ is believed to be a 2-band superconductor as measured in several tunneling and other probe experiments[2,125] with varying gap sizes measured with ARPES from 0.7 to 1.4 meV[126] and the tunneling spectra of bulk NbSe$_2$ has clearly resolved the presence of two superconducting order parameters.[125] This manifests in NbSe$_2$ as a intricate structure of the coherence peaks that differs from standard BCS where shoulders appear at lower energy values than the dominate coherence peaks. In Noat *et. al.*[2] and Dvir *et. al.*,[125] a two-band model is used to fit NbSe$_2$ tunneling data is justified noting that the Se and Nb-derived bands differ in the DOS and value of electron-phonon coupling parameter. The model entails a self-consistent solution to the coupled equations for the energy dependent order parameters $\Delta_i(E)$ in the two bands:

$$\Delta_i(E) = \frac{\Delta_i^0 + \Gamma_{ij}\Delta_j(E)/\sqrt{\Delta_j^2(E) - E^2}}{1 + \Gamma_{ij}/\sqrt{\Delta_j^2(E) - E^2}}. \tag{4.14}$$

Δ_i^0 describes the intrinsic gap within each band generated by scattering of the quasiparticles between bands and the electron-phonon coupling. The DOS of each band is given by

$$N_i(E) = N_i(E_F)\frac{1}{2\pi}\int d\theta\, \Re\left(\frac{|E|}{\sqrt{(1+\alpha\cos\theta)\Delta_i^2(E) - E^2}}\right). \tag{4.15}$$

Where $N_i(E)$ is the DOS at the Fermi level in the normal state. The parameter α, incorporates band-anisotropy which also effects the effective electron temperature fit.

While the DOS is then naturally broadened with kinks indicating two coupled gaps or a highly anisotropic gap,[127] these fitting models introduce additional, partially degenerate broadening channels (interband coupling Γ_{ij} and anisotropy parameter). In practice, broadening in DOS from these extra parameters can trade off against thermal smearing in $f'(E;T_{\text{eff}})$ during fitting. This makes it possible to achieve comparably good fits with artificially *low* fitted T_{eff} by "dumping" spectral width into Γ_{ij} or α.

To avoid this degeneracy when our objective is a robust bound on the electron temperature, we deliberately adopt the simpler, single-gap BCS DOS with either Dynes (lifetime) or Maki (pair-breaking) broadening. This constrained model limits non-thermal broadening channels, so the fitted T_{eff} is biased *high* relative to more flexible multiband/anisotropic fits providing a defensible upper bound on electron temperature.

4.8.5 MAKI FIT TO NBSE$_2$ SUPERCONDUCTING GAP

In Fig. 4.10, we present the fitting of the experimental data presented in Fig. 3.11(c) now using the Maki function for the DOS. The fits present a similar upper bound in the electron temperature (924 mK instead of 950 mK) but a lower bound (775 mK instead of 330 mK). The discrepancy is likely a result of the poor junction stability present during the data collection resulting in a noisy superconducting spectrum plot.

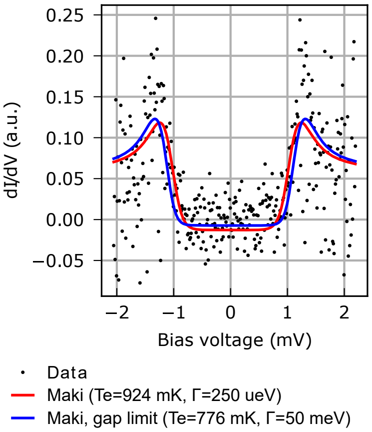

Figure 4.10: Maki function fitting to the superconducting gap spectrum presented in Fig. 3.11(c). A fit allowing for a large range of parameter values is shown in red yielding a higher electron temperature upper bound. Another fit, blue, is presented for the gap size being no smaller than 1.25 meV yielding a lower electron temperature.

References

[1] B. Voigtländer, *Scanning Probe Microscopy* (Springer, Berlin, Heidelberg, 2015).

[2] Y. Noat, J. A. Silva-Guillén, T. Cren, V. Cherkez, C. Brun, S. Pons, F. Debontridder, D. Roditchev, W. Sacks, L. Cario, P. Ordejón, A. García, and E. Canadell, Phys. Rev. B **92**, 134510 (2015).

[3] T. Machida, Y. Sun, S. Pyon, S. Takeda, Y. Kohsaka, T. Hanaguri, T. Sasagawa, and T. Tamegai, Nature Materials 2019 18:8 **18**, 811 (2019).

[4] G. Binnig, C. F. Quate, and C. Gerber, Physical Review Letters **56**, 930 (1986).

[5] E. Meyer, H. Heinzelmann, H. Rudin, and H. J. Güntherodt, Zeitschrift für Physik B Condensed Matter **79**, 3 (1990).

[6] F. J. Giessibl and G. Binnig, Ultramicroscopy **42-44**, 281 (1992).

[7] G. Meyer and N. M. Amer, Applied Physics Letters **53**, 2400 (1988).

[8] Y. Martin and H. K. Wickramasinghe, Applied Physics Letters **50**, 1455 (1987).

[9] R. Erlandsson, G. M. McClelland, C. M. Mate, and S. Chiang, Journal of Vacuum Science & Technology A **6**, 266 (1988).

[10] G. Meyer and N. M. Amer, Rev. Sci. Instrum **56**, 47 (1990).

[11] D. Rugar, H. J. Mamin, and P. Guethner, Applied Physics Letters **55**, 2588 (1989), has a useful figure on fiber-optic inteferometers.

[12] W. H. Rensen, N. F. V. Hulst, A. G. Ruiter, and P. E. West, Applied Physics Letters **75**, 1640 (1999).

[13] F. J. Giessibl, F. Pielmeier, T. Eguchi, T. An, and Y. Hasegawa, Physical Review B **84**, 125409 (2011).

[14] P. J. Mulhern, T. Hubbard, C. S. Arnold, B. L. Blackford, and M. H. Jericho, Review of Scientific Instruments **62**, 1280 (1991).

[15] C. A. Putman, B. G. D. Grooth, N. F. V. Hulst, and J. Greve, Journal of Applied Physics **72**, 6 (1992).

[16] F. J. Giessibl, S. Hembacher, M. Herz, C. Schiller, and J. Mannhart, Nanotechnology **15**, S79 (2004).

[17] F. Mohn, B. Schuler, L. Gross, and G. Meyer, Applied Physics Letters **102**, 073109 (2013).

[18] L. Gross, F. Mohn, N. Moll, P. Liljeroth, and G. Meyer, Science **325**, 1110 (2009).

[19] A. DiCarlo, M. Scheinfein, and R. Chamberlin, Ultramicroscopy **47**, 383 (1992).

[20] A. Spitzig, A. Pivonka, A. Frenzel, J. Kim, C. Ko, Y. Zhou, E. Hudson, S. Ramanathan, J. E. Hoffman, and J. D. Hoffman, Applied Physics Letters **120**, 151602 (2022).

[21] M. Kisiel, E. Gnecco, U. Gysin, L. Marot, S. Rast, and E. Meyer, Nature Materials 2011 10:2 **10**, 119 (2011).

[22] A. J. Czarnecki, N. L. Kolev, P. See, N. J. Sullivan, W. A. Behn, N. J. Curson, T. J. Stock, and P. Grütter, AIP Advances **15**, 105024 (2025).

[23] S. Wirth and P. Schlottmann, Advanced Quantum Technologies **4**, 2100102 (2021).

[24] M. Dzero, K. Sun, V. Galitski, and P. Coleman, Physical Review Letters **104**, 106408 (2010).

[25] M. Dzero, K. Sun, P. Coleman, and V. Galitski, Physical Review B **85**, 045130 (2012).

[26] S. Wolgast, Ç. Kurdak, K. Sun, J. W. Allen, D.-J. Kim, and Z. Fisk, Physical Review B **88**, 180405(R) (2013).

[27] X. Zhang, N. P. Butch, P. Syers, S. Ziemak, R. L. Greene, and J. Paglione, Physical Review X **3**, 011011 (2013).

[28] G. Li, Z. Xiang, F. Yu, T. Asaba, B. Lawson, P. Cai, C. Tinsman, A. Berkley, S. Wolgast, Y. S. Eo, D.-J. Kim, C. Kurdak, J. W. Allen, K. Sun, X. H. Chen, Y. Y. Wang, Z. Fisk, and L. Li, Science **346**, 1208 (2014).

[29] D. J. Kim, S. Thomas, T. Grant, J. Botimer, Z. Fisk, and J. Xia, Scientific Reports **3**, 3150 (2013).

[30] D. J. Kim, J. Xia, and Z. Fisk, Nature Materials **13**, 466 (2014).

[31] Y. Nakajima, P. Syers, X. Wang, R. Wang, and J. Paglione, Nature Physics **12**, 213 (2016).

[32] W. A. Phelan, S. M. Koohpayeh, P. Cottingham, J. W. Freeland, J. C. Leiner, C. L. Broholm, and T. M. McQueen, Physical Review X **4**, 031012 (2014).

[33] P. Syers, D. Kim, M. S. Fuhrer, and J. Paglione, Physical Review Letters **114**, 096601 (2015).

[34] N. Xu, X. Shi, P. K. Biswas, C. E. Matt, R. S. Dhaka, Y. Huang, N. C. Plumb, M. Radović, J. H. Dil, E. Pomjakushina, K. Conder, A. Amato, Z. Salman, D. M. Paul, J. Mesot, H. Ding, and M. Shi, Physical Review B **88**, 121102(R) (2013).

[35] J. Jiang, S. Li, T. Zhang, Z. Sun, F. Chen, Z. R. Ye, M. Xu, Q. Q. Ge, S. Y. Tan, X. H. Niu, M. Xia, B. P. Xie, Y. F. Li, X. H. Chen, H. H. Wen, and D. L. Feng, Nature Communications **4**, 3010 (2013).

[36] M. Neupane, N. Alidoust, S.-Y. Xu, T. Kondo, Y. Ishida, D. J. Kim, C. Liu, I. Belopolski, Y. J. Jo, T.-R. Chang, H.-T. Jeng, T. Durakiewicz, L. Balicas, H. Lin, A. Bansil, S. Shin, Z. Fisk, and M. Z. Hasan, Nature Communications **4**, 2991 (2013).

[37] E. Frantzeskakis, N. de Jong, B. Zwartsenberg, Y. K. Huang, Y. Pan, X. Zhang, J. X. Zhang, F. X. Zhang, L. H. Bao, O. Tegus, A. Varykhalov, A. de Visser, and M. S. Golden, Physical Review X **3**, 041024 (2013).

[38] Z.-H. Zhu, A. Nicolaou, G. Levy, N. P. Butch, P. Syers, X. F. Wang, J. Paglione, G. A. Sawatzky, I. S. Elfimov, and A. Damascelli, Physical Review Letters **111**, 216402 (2013).

[39] J. D. Denlinger, J. W. Allen, J.-S. Kang, K. Sun, J.-W. Kim, J. H. Shim, B. I. Min, D.-J. Kim, and Z. Fisk, arXiv:1312.6637 (2014).

[40] C.-H. Min, P. Lutz, S. Fiedler, B. Y. Kang, B. K. Cho, H.-D. Kim, H. Bentmann, and F. Reinert, Physical Review Letters **112**, 226402 (2014).

[41] N. Xu, P. K. Biswas, J. H. Dil, R. S. Dhaka, G. Landolt, S. Muff, C. E. Matt, X. Shi, N. C. Plumb, M. Radović, E. Pomjakushina, K. Conder, A. Amato, S. V. Borisenko, R. Yu, H.-M. Weng, Z. Fang, X. Dai, J. Mesot, H. Ding, and M. Shi, Nature Communications **5**, 4566 (2014).

[42] S. Rößler, T.-H. Jang, D.-J. Kim, L. H. Tjeng, Z. Fisk, F. Steglich, and S. Wirth, Proceedings of the National Academy of Sciences of the U.S.A. **111**, 4798 (2014).

[43] W. Ruan, C. Ye, M. Guo, F. Chen, X. Chen, G.-M. Zhang, and Y. Wang, Physical Review Letters **112**, 136401 (2014).

[44] C. E. Matt, H. Pirie, A. Soumyanarayanan, Y. He, M. M. Yee, P. Chen, Y. Liu, D. T. Larson, W. S. Paz, J. J. Palacios, M. H. Hamidian, and J. E. Hoffman, Physical Review B **101**, 085142 (2020).

[45] H. Pirie, Y. Liu, A. Soumyanarayanan, P. Chen, Y. He, M. M. Yee, P. F. S. Rosa, J. D. Thompson, D.-J. Kim, Z. Fisk, X. Wang, J. Paglione, D. K. Morr, M. H. Hamidian, and J. E. Hoffman, Nature Physics **16**, 52 (2020).

[46] H. Weng, J. Zhao, Z. Wang, Z. Fang, and X. Dai, Physical Review Letters **112**, 016403 (2014).

[47] M. Xia, J. Jiang, Z. R. Ye, Y. H. Wang, Y. Zhang, S. D. Chen, X. H. Niu, D. F. Xu, F. Chen, X. H. Chen, B. P. Xie, T. Zhang, and D. L. Feng, Scientific Reports **4**, 5999 (2014).

[48] N. Xu, C. E. Matt, E. Pomjakushina, J. H. Dil, G. Landolt, J.-Z. Ma, X. Shi, R. S. Dhaka, N. C. Plumb, M. Radovic, V. N. Strocov, T. K. Kim, M. Hoesch, K. Conder, J. Mesot, H. Ding, and M. Shi, arXiv:1405.0165 (2014).

[49] M. Neupane, S.-Y. Xu, N. Alidoust, G. Bian, D. J. Kim, C. Liu, I. Belopolski, T.-R. Chang, H.-T. Jeng, T. Durakiewicz, H. Lin, A. Bansil, Z. Fisk, and M. Z. Hasan, Physical Review Letters **114**, 016403 (2015).

[50] E. Frantzeskakis, N. de Jong, J. X. Zhang, X. Zhang, Z. Li, C. L. Liang, Y. Wang, A. Varykhalov, Y. K. Huang, and M. S. Golden, Physical Review B **90**, 235116 (2014).

[51] Z. Xiang, Y. Kasahara, T. Asaba, B. Lawson, C. Tinsman, L. Chen, K. Sugimoto, S. Kawaguchi, Y. Sato, G. Li, S. Yao, Y. L. Chen, F. Iga, J. Singleton, Y. Matsuda, and L. Li, Science **362**, 65 (2018).

[52] T. Zhang, G. Li, S. C. Sun, N. Qin, L. Kang, S. H. Yao, H. M. Weng, S. K. Mo, L. Li, Z. K. Liu, L. X. Yang, and Y. L. Chen, Chinese Physics B **29**, 017304 (2020).

[53] J. M. Tarascon, J. Etourneau, P. Dordor, P. Hagenmuller, M. Kasaya, and J. M. D. Coey, Journal of Applied Physics **51**, 574 (1980).

[54] T. Nanba, M. Tomikawa, Y. Mori, N. Shino, S. Imada, S. Suga, S. Kimura, and S. Kunii, Physica B: Condensed Matter **186-188**, 557 (1993).

[55] A. Kakizaki, A. Harasawa, T. Kinoshita, T. Ishii, T. Nanba, and S. Kunii, Physica B: Condensed Matter **186-188**, 80 (1993).

[56] T.-R. Chang, T. Das, P.-J. Chen, M. Neupane, S.-Y. Xu, M. Z. Hasan, H. Lin, H.-T. Jeng, and A. Bansil, Physical Review B **91**, 155151 (2015).

[57] C.-J. Kang, J. D. Denlinger, J. W. Allen, C.-H. Min, F. Reinert, B. Y. Kang, B. K. Cho, J.-S. Kang, J. H. Shim, and B. I. Min, Physical Review Letters **116**, 116401 (2016).

[58] S. Ramankutty, N. de Jong, Y. Huang, B. Zwartsenberg, F. Massee, T. Bay, M. Golden, and E. Frantzeskakis, Journal of Electron Spectroscopy and Related Phenomena **208**, 43 (2016).

[59] E. Berg, M. S. Rudner, and S. A. Kivelson, Physical Review B **85**, 035116 (2012).

[60] Y. A. Bychkov and E. I. Rashba, Journal of Physics C: Solid State Physics **17**, 6039 (1984).

[61] M. K. Blomberg, M. J. Merisalo, M. M. Korsukova, and V. N. Gurin, Journal of Alloys and Compounds **217**, 123 (1995).

[62] J. Etourneau, J.-P. Mercurio, R. Naslain, and P. Hagenmuller, Journal of Solid State Chemistry **2**, 332 (1970).

[63] The expected YbB_6 lattice constant of $a = 4.1439$ Å was inferred from the room-temperature value $a = 4.1479$ Å measured by x-ray diffraction on single crystals of YbB_6 [61], and the thermal contraction of 0.096% from room temperature to 4 K, measured in other rare-earth hexaborides [62]. After verifying $\sim 5\%$ consistency with our independent rough calibration, all topographies are displayed with refined calibration using the exact value $a = 4.1439$ Å.

[64] C. Tournier-Colletta, G. Autès, B. Kierren, P. Bugnon, H. Berger, Y. Fagot-Revurat, O. V. Yazyev, M. Grioni, and D. Malterre, Physical Review B **89**, 085402 (2014).

[65] I. Battisti, V. Fedoseev, K. M. Bastiaans, A. de la Torre, R. S. Perry, F. Baumberger, and M. P. Allan, Physical Review B **95**, 235141 (2017).

[66] L. Fu, C. L. Kane, and E. J. Mele, Physical Review Letters **98**, 106803 (2007).

[67] L. Fu and C. L. Kane, Physical Review B **76**, 045302 (2007).

[68] C. R. Ast, G. Wittich, P. Wahl, R. Vogelgesang, D. Pacilé, M. C. Falub, L. Moreschini, M. Papagno, M. Grioni, and K. Kern, Physical Review B **75**, 201401(R) (2007).

[69] M. F. Crommie, C. P. Lutz, and D. M. Eigler, Nature **363**, 524 (1993).

[70] L. Kong, S. Zhu, M. Papaj, H. Chen, L. Cao, H. Isobe, Y. Xing, W. Liu, D. Wang, P. Fan, Y. Sun, S. Du, J. Schneeloch, R. Zhong, G. Gu, L. Fu, H. J. Gao, and H. Ding, Nature Physics 2019 15:11 **15**, 1181 (2019).

[71] S. Zhu, L. Kong, L. Cao, H. Chen, M. Papaj, S. Du, Y. Xing, W. Liu, D. Wang, C. Shen, F. Yang, J. Schneeloch, R. Zhong, G. Gu, L. Fu, Y.-Y. Zhang, H. Ding, and H.-J. Gao, Science **367**, 189 (2020).

[72] D. Wang, L. Kong, P. Fan, H. Chen, S. Zhu, W. Liu, L. Cao, Y. Sun, S. Du, J. Schneeloch, R. Zhong, G. Gu, L. Fu, H. Ding, and H.-J. Gao, Science **362**, 333 (2018).

[73] A. Ghiotto, E. M. Shih, G. S. Pereira, D. A. Rhodes, B. Kim, J. Zang, A. J. Millis, K. Watanabe, T. Taniguchi, J. C. Hone, L. Wang, C. R. Dean, and A. N. Pasupathy, Nature **597**, 345 (2021).

[74] Y. Cao, V. Fatemi, S. Fang, K. Watanabe, T. Taniguchi, E. Kaxiras, and P. Jarillo-Herrero, Nature **556**, 43 (2018).

[75] Y. Choi, J. Kemmer, Y. Peng, A. Thomson, H. Arora, R. Polski, Y. Zhang, H. Ren, J. Alicea, G. Refael, F. von Oppen, K. Watanabe, T. Taniguchi, and S. Nadj-Perge, Nature Physics **15**, 1174 (2019).

[76] H. Zhao, H. Li, B. R. Ortiz, S. M. Teicher, T. Park, M. Ye, Z. Wang, L. Balents, S. D. Wilson, and I. Zeljkovic, Nature **599**, 216 (2021).

[77] H. H. Sun, K. W. Zhang, L. H. Hu, C. Li, G. Y. Wang, H. Y. Ma, Z. A. Xu, C. L. Gao, D. D. Guan, Y. Y. Li, C. Liu, D. Qian, Y. Zhou, L. Fu, S. C. Li, F. C. Zhang, and J. F. Jia, Physical Review Letters **116**, 257003 (2016).

[78] S. Jeon, Y. Xie, J. Li, Z. Wang, B. A. Bernevig, and A. Yazdani, Science **358**, 772 (2017).

[79] J. F. Schooley, W. R. Hosler, and M. L. Cohen, Physical Review Letters **12**, 474 (1964).

[80] W. Wigglesworth, (2013), provides simulations of performance degradation due to stacked passive air leg isolators as mass ratios become wider between stages.

[81] W. Gong, Y. Liu, W.-T. Liao, J. Gibbons, and J. E. Hoffman, Review of Scientific Instruments **92**, 013703 (2021).

[82] ND40-A Elastomeric Isolation Mount, Newport Corporation, Irvine CA.

[83] 871239-01, PD-Series, Integrated Dynamics Engineering, Inc., Mansfield MA.

[84] High Field Liquid Helium Magnet System, Cryogenic US LLC, Seattle WA.

[85] JDR-500-TL-JT-UHV-SPM Dilution Refrigerator System, FormFactor, Inc., Livermore CA.

[86] McAllister Technical Services, Coeur d'Alene ID.

[87] 095-190-NT-20, spherical u contact Series, Omega Shielding, Inc., Randolph NJ.

[88] G. Balint, B. Antala, C. Carty, J.-M. A. Mabieme, I. B. Amar, and A. Kaplanova, National Institute of Standards and Technology .

[89] N. J. Simon, E. S. Drexler, and R. P. Reed, NIST Monograph **177** (1992).

[90] L. R. Powell and A. W. Blanpied, National Bureau of Standards Circular **556** (1954).

[91] D. R. Smith and F. R. Fickett, Journal of Research of the National Institute of Standards and Technology **100**, 119 (1995).

[92] P. Pierini, CERN Accelerator School: High Power Hadron Machines, CAS 2011 - Proceedings , 349 (2013).

[93] E. R. Dobrovinskaya, L. A. Lytvynov, and V. Pishchik, Sapphire , 55 (2009).

[94] Corning Incorporated .

[95] M. Omini and A. Sparavigna, Physical Review B **61**, 6677 (2000).

[96] N. V. Kozyrev, International Journal of Thermophysics **45**, 37 (2024).

[97] N. Simon, NISTIR **5030** (1994).

[98] D. Rule and L. Sparks, NISTIR **89-3914** (1989).

[99] X. X. Chu, Z. X. Wu, R. J. Huang, Y. Zhou, and L. F. Li, Cryogenics **50**, 84 (2010).

[100] S. H. Pan, WO/1993/019494.

[101] 903-1229-ND, Fingerstock BeCu, Laird Technologies EMI.

[102] RX-102A-BR, Rox 102A bare chip RTD, Lake Shore Cryotonics, Inc., Westerville OH.

[103] Micro 360(R) Plastic Circular Straight Tail, Omnetics Connector Corp, Minneapolis MN.

[104] J. Schwenk, S. Kim, J. Berwanger, F. Ghahari, D. Walkup, M. R. Slot, S. T. Le, W. G. Cullen, S. R. Blankenship, S. Vranjkovic, H. J. Hug, Y. Kuk, F. J. Giessibl, and J. A. Stroscio, Review of Scientific Instruments **91**, 71101 (2020).

[105] A. Lukashenko and A. V. Ustinov, Review of Scientific Instruments **79**, 14701 (2008).

[106] 752-118-37, Cu80/Sn20 powder, GoodFellow Corp., Coraopolis, PA.

[107] 956-581-15, Inconel 625 powder, GoodFellow Corp., Coraopolis, PA.

[108] 876-168-51, Stainless Steel 316 powder, GoodFellow Corp., Coraopolis, PA.

[109] F. J. Giessibl, Review of Scientific Instruments **90**, 11101 (2019).

[110] Nickel STM Probes, SPECS TII, Inc., Mansfield MA.

[111] PL-NL-0633-B-A8-1-SA, 633nm SM Narrow Linewidth Laser Diode, LD-PD, Inc., Singapore.

[112] LDC501, Laser diode controller, Stanford Research Systems, Inc., Sunnyvale CA.

[113] VOA630-APC, SM Variable Attenuator, Thor Labs, Inc., Newton NJ.

[114] Ascentta, Inc., Somerset NJ.

[115] FPD510-FC-VIS, Si Fixed Gain, High Sensitivity PIN Amplified Detector, Thor Labs, Inc., Newton NJ.

[116] ASI4.3/125/145T, Single Mode, Silica Core/Silica Clad/Thermocoat Coating, Fiberguide Industries, Inc., Caldwell ID.

[117] LDM-4984, Laser Diode Mount, 14-pin Butterfly, Newport Corporation, Irvine CA.

[118] R. C. Dynes, V. Narayanamurti, and J. P. Garno, Physical Review Letters **41**, 1509 (1978).

[119] Y. Que, A. Kumar, M. S. Lodge, Z. Tong, M. K. F. Lai, W. Tao, Z. Cui, R. Shivajirao, J. Jia, S. E. Lee, and B. Weber, Nanotechnology **34**, 455704 (2023).

[120] D. Wong, S. Jeon, K. P. Nuckolls, M. Oh, S. C. J. Kingsley, and A. Yazdani, Review of Scientific Instruments **91**, 23703 (2020).

[121] E. C. Jordan, *Electromagnetic waves and radiating systems* (Prentice-Hall, New York, 1950).

[122] T. Machida, Y. Kohsaka, . T. Hanaguri, . Y. Kohsaka, and T. Hanaguri, Rev. Sci. Instrum **89**, 93707 (2018).

[123] K. Maki, Progress of Theoretical Physics **32**, 29 (1964).

[124] M. Assig, M. Etzkorn, A. Enders, W. Stiepany, C. R. Ast, and K. Kern, Review of Scientific Instruments **84**, 033903 (2013).

[125] T. Dvir, F. Massee, L. Attias, M. Khodas, M. Aprili, C. H. Quay, and H. Steinberg, Nature Communications **9**, 598 (2018).

[126] D. J. Rahn, S. Hellmann, M. Kalläne, C. Sohrt, T. K. Kim, L. Kipp, and K. Rossnagel, Phys. Rev. B **85**, 224532 (2012).

[127] A. J. Bennett, Physical Review **140**, A1902 (1965)